9-26-2018

Effect of Aspect Ratio on the Flow Structures Behind a Square Cylinder

Junting Chen
University of Windsor

Effect of Aspect Ratio on the Flow Structures Behind a Square Cylinder

By

Junting Chen

A Thesis

Submitted to the Faculty of Graduate Studies
through the Department of Mechanical, Automotive and Materials Engineering in Partial Fulfillment of the Requirements for the Degree of Master of Applied Science at the University of Windsor

Windsor, Ontario, Canada

2018

Effect of Aspect Ratio on the Flow Structures Behind a Square Cylinder

by

Junting Chen

APPROVED BY:

_____

S.Cheng
Department of Civil and Environmental Engineering

_____

D.Ting
Department of Mechanical, Automotive and Materials Engineering

_____

R.Barron, Co-Advisor
Department of Mechanical, Automotive and Materials Engineering

_____

R.Balachandar, Co-Advisor
Department of Mechanical, Automotive and Materials Engineering

September 25th, 2018

Author's Declaration of Originality

I hereby certify that I am the sole author of this thesis and that no part of this thesis has been published or submitted for publication

I declare that, to the best of my knowledge, my thesis does not infringe up on anyone's copyright nor violate any proprietary rights and that any ideas, techniques, quotations, or any other material from the work of other people included in my thesis are fully acknowledged in accordance with the standard referencing practices. Furthermore, to the extent that I have included copyrighted material that surpasses the bounds of fair dealing within the meaning of the Canada copyright Act.

I declare that this is the true copy of my thesis, including any final revisions, as approved by my thesis committee and the Graduate Studies office, and that this thesis has not been submitted for a higher degree to any other University or Institution.

Abstract

In this thesis, the effect of aspect ratio on the flow past square cross-section wall-mounted cylinders is evaluated using computational fluid dynamics. The simulations are carried out using the Improved Delayed Detached Eddy (IDDES) turbulence model. Three cases with different heights of the cylinder (aspect ratio = cylinder height/width = 1, 2, and 4) were studied. The IDDES prediction of the flow statistics is validated against a set of wind tunnel experimental results from a recent report on the flow at a Reynolds number of 12,000 for a cylinder aspect ratio of four.

It is common practise to analyse results in different horizontal and vertical planes in the wake of the bluff body. To this end, the traditional methods use a geometrical scaling factor such as the height/diameter of the cylinder or depth of flow. However, this can lead to an improper analysis as one may not capture the flow properties based on the physics of the flow. The flow characteristics can be influenced by both the proximity to the bed and to the cylinder's free-end. In this thesis, a new method, based on the flow physics, is proposed to evaluate the role of aspect ratio using the forebody pressure distribution.

Using the turbulence features and vortex identification methods, it is observed that the flow structure is influenced by the aspect ratio. The downwash flow noticed in the wake tends to become less dominant with increasing aspect ratio, accompanied by a near-bed upwash flow at the rear of the cylinder. The mean and instantaneous flow field characteristics at each aspect ratio has been examined and compared in different planes to

elucidate their three-dimensional features. The far-wake of each flow field is visualized and examined using the three-dimensional iso-surface of the λ_2 criterion.

Dedication

To my parents, Zhi Chen and Wei Wang,

and my sister Xinyi Chen

Acknowledgements

This research was made possible by the facilities of the Shared Hierarchical Academic Research Computing Network (SHARCNET: www.sharcnet.ca) and Compute/Calcul Canada.

I would like to express my heartiest thanks to my advisors, Dr. Balachandar and Dr. Barron, for their immense support and guiding me on every aspect throughout my thesis work. Without their encouragement and advice, I would not have been able to successfully complete it. I would also like to thank my committee members Dr. S. Cheng and Dr. D. Ting.

I would also like to thank Dr. Kohei Fukuda, Dr. Vimaldoss Jesudhas and Dr. Vesselina Roussinova for sharing their knowledge with me during my study. Also, I would like to thank all of my colleagues, Sudharsan Annur Balasubramanian, Sachin Sharma, Shu Chen, Subhadip Das, Nimesh Virani, Priscilla Williams, Kharuna Ramrukheea, Chris Peirone, Yuanming Yu and Elle Mistruzzi for sharing their moments during my study.

Table of Contents

List of Figures

Nomenclature

AR	Aspect ratio (-)
C_p	Pressure coefficient (-)
d	Cylinder width (m)
d_{wall}	Distance to the nearest wall (m)
E	Energy (J)
f	IDDES blending function (-)
h	Cylinder height (m)
k	Turbulence kinetic energy (m^2/s^2)
p	Static pressure (Pa)
P_0	Atmospheric pressure (Pa)
P_{stag}	Pressure at the stagnation point (Pa)
R_β, R_ω and R_k	Closure coefficients in viscous damping functions (-)
Re_d	Reynolds number based on the cylinder width (-)
Re_θ	Reynolds number based on the boundary layer thickness (-)
Re_T	Turbulent Reynolds number (-)
S_T	Stress tensor (Pa)
St	Strouhal number (-)
t	Time (s)
u_τ	Friction velocity (m/s)
u, v, w	Fluctuating velocity components in x, y, z direction (m/s)
U_0	Freestream velocity (m/s)
U_s	Approach velocity at the corresponding location (m/s)
U_{max}	Maximum velocity (m/s)
U_i and $\overline{U}_i$	Instantaneous and time-averaged velocity in tensor notation (m/s)
U, V, W	Instantaneous velocity components in x, y, z direction (m/s)
$\overline{U}, \overline{V}, \overline{W}$	Time-averaged velocity components in x, y, z direction (m/s)
$\frac{\sqrt{\overline{u^2}}}{U_0}, \frac{\sqrt{\overline{v^2}}}{U_0}, \frac{\sqrt{\overline{w^2}}}{U_0}$	Turbulence intensities in x, y, z direction (-)

x_i	Position vector in tensor notation (m)
x, y, z	Cartesian axis directions (m)
z^+	Normalized wall normal distance (-)
λ_2	Second eigenvalue of the pressure Hessian matrix (-)
ε	Turbulence dissipation rate (m^2/s^2)
$\emptyset, \overline{\emptyset}, \emptyset'$	A scalar quantity, time-averaged and fluctuation of this quantity
ρ	Fluid density (kg/m^3)
$\widetilde{\tau}$	Reynolds stress tensor (Pa)
μ	Dynamic viscosity (m^2/s)
μ_T	Eddy viscosity (m^2/s)
υ	Kinematic viscosity (m^2/s)
ω	Specific dissipation rate (1/s)
$\Omega_x, \Omega_y, \Omega_z$	Vorticity in x, y, z direction (1/s)
Ω_T	Rotational tensor (1/s)

Chapter 1 Introduction

A wall-mounted finite-length cylinder immersed in a flow produces a flow field that is representative of that observed in many engineering applications in the real world, such as wind flow past low-rise buildings, flow past electronic components and cooling towers. The interaction between the fluid and the cylinder creates complex flow field structures in the near wall region and in the turbulent wake behind the cylinder. The flow structures greatly influence the performance of such a system with respect to, for example, pedestrian comfort along a city street, heat transfer rate for electronic cooling, or prediction of pollutant dissipation. It is also important to accurately predict the shedding frequency of the vortices that develop behind the cylinder in order to avoid vibration induced by resonance. Therefore, it is necessary to acquire an in-depth understanding of wall-mounted bluff body flow in order to make improvements in practical application of such flows.

The flow structure is mainly determined by three factors; Reynolds number (Re_d), aspect ratio (AR = h/d, where h and d are the height and width of the cylinder, respectively), and the relative boundary layer thickness (δ/d) [1]. At a low Reynolds number, viscous forces dominate over inertial forces. In this case, the flow field tends to be steady and very little turbulence is observed. As the Reynolds number increases, inertial forces overcome the viscous forces and dominate the flow field. The flow field becomes turbulent and more complex flow structures appear. El Hassan et al. [2] experimentally studied the effect of relative boundary layer thickness on the flow field around the square cylinder with AR = 4. They confirmed that the wake size is influenced by the boundary layer, and observed a vortex street that formed behind the body. A

similar conclusion was found by Wang and Zhou [3]. It was concluded that as the boundary layer thickness increases, the strength of the upwash flow behind the body is enhanced, thereby weakening the effect of the downwash flow from the free-end of the square cylinder.

The effect of aspect ratio of the cylinder on the flow field requires further investigation. A critical value of AR, which is differentiated by the induced wake structures, has been found to lie between the value of 3 and 5 [4]. Wang and Zhou [3] showed that the flow past a cylinder with AR below the critical value is more likely to create a symmetric arch-type wake, and that the flow past a cylinder with AR above such value is more likely to create a wake similar to an asymmetric von Kármán vortex street. An in-depth comparison of the flow field near the square cylinders below and approaching the critical aspect ratio has not been established so far. In the current research, the Reynolds number (Re_d) and boundary layer thickness (δ) of the incoming flow will be fixed, and the square cylinders studied in this research have aspect ratios of 1, 2 and 4.

This research is conducted numerically with the commercial code Star-CCM+ v11.04 [5], running on the high-performance computing environment Shared Hierarchical Academic Research Computing Network (SHARCNET). The first phase of this research project is to validate the simulation model using the experimental results of El Hassan et al. [2] at the cylinder aspect ratio of 4. After that, in the second phase, flow past a square cylinder with AR = 1 and 2 are examined and compared to the square cylinder with AR = 4.

The objectives of this research project are:

1. to model and validate the flow over a wall-mounted finite-length square cylinder with the aspect ratio of four, using the Detached-Eddy Simulation turbulence model;
2. to study the wake structure and the interaction between the vortical structures around the square cylinder at different aspect ratios;
3. to provide an alternative method for horizontal plane selection which allows researchers to better examine and compare the flow field around cylinders at different aspect ratios.

This thesis consists of four chapters. Chapter 1 provides a brief introduction to the problem; Chapter 2 gives an overview of previous studies conducted on related problems and discusses the turbulence model selection. Chapter 3 focuses on the numerical model and grid setup, including the grid independence study and the validation of the model. Chapter 4 discusses the simulation results. The time-averaged results on the vertical planes and horizontal planes will be presented. Then, instantaneous turbulent quantities are examined in order to gain a better understanding of the effect of aspect ratio on the vortical structures and other features of the flow field.

Chapter 2 Literature Review and Mathematical Model

2.1 Introduction

In this chapter, the relevant studies that have been conducted on this topic are discussed. Previous experimental work has been used to obtain a general overview of the physics of the flow field; the numerical work contributes to the model setup and provides an understanding of the details in the flow field that was not obtained in the experiments. The governing equations are also introduced in this chapter, along with a brief introduction of the turbulence modeling applied to the current study.

2.2 Previous Experimental Studies

The flow over a square cylinder has been experimentally studied in terms of evaluating characteristics of the vortical structures in the flow field. The flow structure is mainly determined by three factors; Reynolds number based on the approach flow velocity and cylinder width (Re_d), aspect ratio (AR = h/d, where h and d, are the height and width of the cylinder, respectively), and the boundary layer thickness of the approach flow (δ). The flow field structure around a wall-mounted cube was studied experimentally by Castro and Robins [6]. To assess the effect of the approach flow, they compared an incoming sheared turbulent flow with an irrotational uniform flow and observed that the turbulent incoming flow tended to induce a smaller wake region. They

also found that the decay of velocity deficit behind the cube was strongly influenced by turbulence intensity, as subsequently confirmed by Hunt et al. [7].

Lin et al. [1] performed an extensive study to determine how Re_d, δ and AR influence the horseshoe vortex (HSV) system formed in front of the body for various Reynolds numbers ($200 < Re_d < 6{,}000$) considering the flow over a wall-mounted finite-height square cylinder. They identified four regimes in the HSV: a steady horseshoe, periodic oscillation with small displacement, periodic breakaway vortex system and irregular vortex system. This categorization was found to be strongly correlated with h/δ and Re_d.

To determine the effect of the approach flow boundary layer thickness, Wang et al. [8] studied the flow over a square cylinder with three different values of δ. They noted the flow field to be highly three-dimensional and consisted of the vortical structures which included the tip vortex (connected to the downwash flow), the spanwise vortex (the von Kármán vortex street), the base vortex formed at the junction of the wall and the cylinder base, an upwash flow and the horseshoe vortex. A cartoon illustrating the fluid structures is shown in Figure 1. The upwash flow in the wake was found to be enhanced with increasing boundary layer thickness, and the downwash flow near the free-end shear layer was consequently weakened by the enhanced upwash flow. As the upwash flow developed, the base section of it moved towards the leeward face of the cylinder.

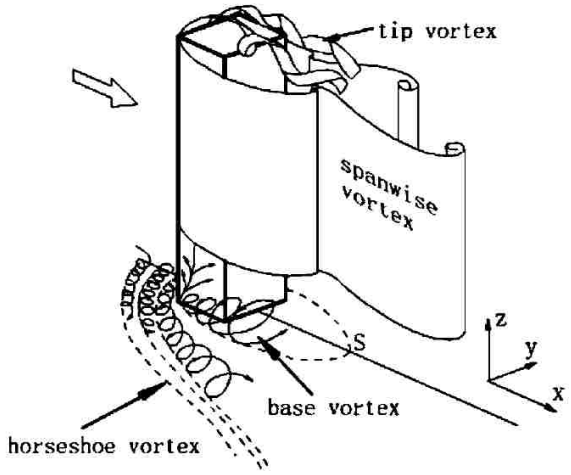

Figure 2.1 Schematic of the flow structure behind a wall-mounted finite square cylinder with AR > 5 [8]

Wang and Zhou [3] studied the flow past a square cylinder with various aspect ratios for $Re_d = 9300$, $\delta/d = 1.35$. From their experimental study, they concluded that the size of the reverse flow zone behind the cylinder was largely dependent on the cylinder AR when the aspect ratio was between 3 and 7. Within this range, both upwash and downwash flow in the wake were increased with increasing AR. In their study, Wang and Zhou [3] presented a more sophisticated model with two different configurations of the arch-type vortex forming behind the square cylinder. An asymmetric configuration dominated the wake when the cylinder AR exceeded a critical value (between 3 and 5), while symmetric spanwise vortical structures were found to be dominant when the AR was smaller than the critical value.

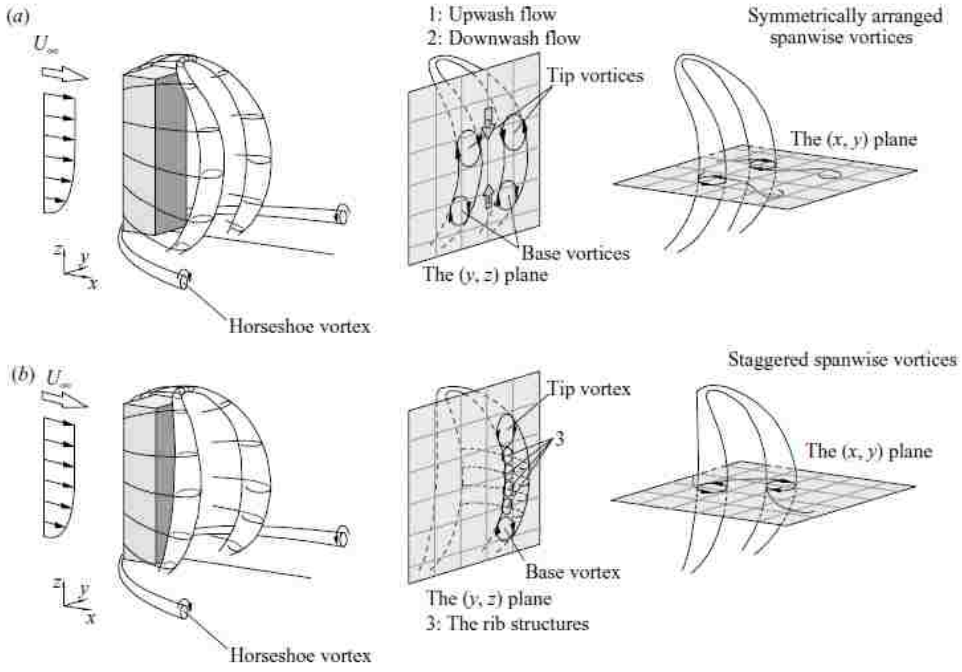

Figure 2.2 Schematic of the flow structure around a wall-mounted finite square cylinder: (a) two symmetric spanwise vortices, (b) asymmetric spanwise vortices [3]

Bourgeois et al. [9] conducted an experimental investigation of air flow with a thin boundary layer over a wall-mounted finite-height square cylinder. The flow field near a square cylinder with AR = 4 was captured using a laser Doppler velocimeter (LDV). This flow field served as a challenge problem at the CFD Society of Canada Annual Conference in 2012, and the LDV results were used to benchmark the numerical solutions submitted by participants. This study showed that the alternating vortex shedding was deformed due to the free-end shear layer as it evolved downstream. The flow field was decomposed by phase averaging, which captured the coherent and incoherent structures in the flow field. Later, El Hassan et al. [2] continued this investigation to study the effect of the boundary layer thickness on the wake structures. They observed that the upwash in the wake flow increased as the boundary layer became

thicker, similar to the observation of Wang and Zhou [3]. In the thinner boundary layer case, the influence of the horseshoe vortex on the wake region was limited and as δ increased, the entire wake structure was affected by the horseshoe vortex. Sumner et al. [4] summarized the previous studies on flow past a wall-mounted finite circular cylinder and stated that the studies on this topic are insufficient at the present time.

Sumner et al. [4] summarized the previous studies on flow past a wall-mounted finite circular cylinder and stated that the studies on this topic are insufficient at present.

"Apart from the location of the reattachment point, the influences of Reynolds number, aspect ratio, and relative boundary layer thickness are not well understood… …most of the experiments in the literature have been concentrated on cylinders of relatively low aspect ratio, AR ≤ 2, and there is a need for additional studies at higher AR."

- D. Sumner

2.3 Previous Numerical Studies

Shah and Ferziger [10] demonstrated the capability of utilizing the Large-Eddy Simulation (LES) model in the flow past a wall-mounted cube with Reynolds number of 40,000. They showed that the mean and fluctuating quantities at different locations in the flow field matched well with experimental results. Rodi [11] conducted a comparative study on LES and Reynolds Averaged Navier-Stokes (RANS) turbulence models in the case of flow past a wall-mounted square cylinder. All RANS models significantly under-predicted the velocity fluctuations in the flow field. On the other hand, the LES model was capable of capturing the flow characteristics not captured in RANS models, even

though the unsteady RANS model could accurately predict the vortex shedding frequency. However, although the LES calculations increased the computing time by a factor of almost 40 compared with the RANS models, none of the LES results were entirely satisfactory possibly due to the insufficient of resolution on the side-wall of the cylinder. Fröhlich and Rodi [14] numerically studied the vortex shedding process using LES for flow past a finite-height wall-mounted circular cylinder with an aspect ratio of 2.5. Their study revealed the interaction of the separating shear layer from the side wall with that from the free-end. The two-dimensional alternating vortex shedding was distorted as they travelled downstream. The simulation predicted an arch-type vortex behind the cylinder.

Nishino et al. [12] conducted numerical simulation using unsteady RANS and DES for flow past a circular cylinder placed near and parallel to the bed with various gaps. The unsteady RANS model was not capable of predicting the ground effect while the DES result showed a good match with experimental results, by examining the cessation of large-scale alternating vortex shedding behind the cylinder. The authors also noted that the vortical structures resolved in the unsteady RANS were much coarser than those by the DES, although the same grid was employed and the same computational cost was required for each. A significant improvement in the simulation with DES model was displayed over that with unsteady RANS model. Nasif et al. [13] modeled the flow past a sharp edge bluff body in a shallow open channel with DES. The flow field was visualized by creating an iso-surface of the λ_2 – criterion. Various vortical structures in the near-wake and far-wake were identified by the authors.

An in-depth comparison of the flow field near the square cylinders below and approaching the critical aspect ratio has not been established so far. In the current

research, the Reynolds number (Re_d) and boundary layer thickness (δ) of the incoming flow are fixed, while the aspect ratio was varied from 1 to 4. The principal objective of this research project was to study the wake structure and the interaction between the vortical structures around the square cylinder at different aspect ratios. The study also focussed on developing an alternative method for horizontal plane selection to visualise the flow field which would allow researchers to better examine and compare the flow field around cylinders at different ARs.

2.4 Governing Equations and Turbulence Modeling Techniques

The mathematical model of fluid flow and heat transfer is developed from the conservation of mass, Newton's second law and the first law of thermodynamics. After adequate treatment to these general physics laws, they become the continuity equation, momentum equation, and conservation of energy equation. In the conservative form, they are expressed by:

Continuity equation:

$$\frac{\partial \rho}{\partial t} + \ div(\rho U_i) = 0 \tag{2.1}$$

Momentum (Navier-Stokes) equations:

$$\frac{\partial}{\partial t}(\rho U_i\ ) + div(\rho U_i U_i) = -\frac{\partial p}{\partial x} + div(\tilde{\tau}) + \rho g_i \tag{2.2}$$

Conservation of energy:

$$\frac{\partial}{\partial t}(\rho E) + div(\rho E U_i) = -div(p U_i) + grad(k\ grad\ T) + grad(U_i \cdot \tilde{\tau}) \tag{2.3}$$

The definition of the parameters in these equations is given in the Nomenclature. Although heat transfer of flow passing a square cylinder can be studied, the current study only focuses on the flow field structure and physics of the flow field. Therefore the energy equation will not be discussed further.

The solution of the governing flow equations can be decomposed into time-averaged and fluctuating components:

$$\vec{u} = \overline{U} + u \tag{2.4}$$

$$\emptyset = \overline{\emptyset} + \emptyset \tag{2.5}$$

where $\emptyset$ represents any scalar quantity, the overbar notation represents the mean value, and the prime symbol represents the fluctuating component.

Using Equations 2.4 and 2.5, the time-averaged continuity equation and momentum equation for incompressible flow are expressed as:

$$\frac{\partial \overline{U}_i}{\partial x_i} = 0 \tag{2.6}$$

$$\rho \bar{u}_j \frac{\partial \overline{U}_i}{\partial x_j} = -\frac{\partial \bar{p}}{\partial x_i} + \mu \frac{\partial}{\partial x_j}\left(\frac{\partial \overline{U}_i}{\partial x_j} + \frac{\partial \overline{U}_j}{\partial x_i}\right) + \left[-\rho \frac{\partial}{\partial x_j}\left(\overline{u_i u_j}\right)\right] + \rho \vec{g}_i \tag{2.7}$$

The second last term $\left[-\rho \frac{\partial}{\partial x_j}\left(\overline{u_i u_j}\right)\right]$ in the time-averaged momentum equation (2.7) contains the fluctuating components, known as the Reynolds stresses. This term must be computed in turbulent flow and is the main source of difficulties in modeling such flows [15].

The most common approaches to simulate turbulent flow are Reynolds Averaged Navier-Stokes (RANS) models, Large Eddy Simulation (LES) model and hybrid-LES-

RANS, known as the Detached Eddy Simulation (DES) model [16]. The definition of a complete turbulence model is one which "can be used to predict properties of a given turbulent flow with no prior knowledge of the turbulence structure" [17]. Although RANS models have several options including the 0-, 1/2- and 1-equation models, only the k-ϵ and k-ω two-equation models are considered as complete RANS models. In addition to the transport equation for turbulence kinetic energy (k), the k-ω models consist of a second transport equation for specific dissipation rate (ω), while k-ϵ models consist of a transport equation for dissipation rate (ϵ). Over decades of benchmarking these two models, the standard k-ϵ model is known to be sensitive in the near-wall region and the standard k-ω model is sensitive to the inlet freestream turbulence properties. Mentor [18] developed the idea of combining these two turbulence models in order to include the advantages of each, and showed that k-ω shear stress transport (SST) performs better than k-ϵ when an adverse pressure gradient occurs.

Since all the RANS models utilize the Boussinesq eddy viscosity assumption to model velocity fluctuations, the value of turbulence kinetic energy is assumed to be the same in all three directions (x, y, and z). Although this is a convenient way of modeling turbulence and providing a robust prediction, the commonly known drawbacks of RANS (including unsteady RANS) models are:

1. Lack of potential for further analysis of the turbulence quantities
2. Lack of accuracy when adverse pressure gradients exist (although better than k-ϵ, k-ω SST over-predicts turbulence quantities)

The Large Eddy Simulation (LES) model explicitly resolves the large eddies in a simulation and treats the small eddies with sub-grid-scale (SGS) models. The mechanics

behind an LES model can be understood as follows: the large eddies in the flow field are geometry dependent, so the Navier-Stokes equations can be solved directly, and the smaller eddies can be modeled (with Boussinesq eddy viscosity assumption) since they are treated as isotropic. Shah and Ferziger [10] showed that with appropriate grid utilization, an LES model is capable of accurately simulating the flow past a wall-mounted cube. With the LES model, details of turbulence quantities can be acquired as opposed to RANS models in which only time-averaged information is available. However, an LES model requires large computational resources. In order to successfully predict the flow field with an LES model, the computational grid must be carefully designed because of the filtering process. With an inadequate grid setup in the near-wall region, the result of an LES simulation can potentially be much less accurate than any RANS simulation. RANS models are commonly understood as naturally independent of grid spacing, while LES requires the grid spacing to meet a specific standard in order to produce meaningful results [19].

Detached Eddy Simulation (DES) is a hybrid scheme which implements a RANS model in the near-wall region (which allows more flexibility on the grid spacing), and employs an LES model to resolve the large unsteady eddies away from the wall. Only the RANS models which appropriately define the turbulence length scale can be considered in the DES model, such as Spalart-Allmaras (S-A) and k-ω SST. Spalart et al. [20] introduced an Improved Delayed Detached Eddy Simulation (IDDES), which improves the computation at the cells where the transition between the RANS and LES models occurs. A blending function f is used to switch between the selected unsteady RANS and the LES model. The blending function is defined by:

$$f = \min[2exp(-9{\alpha_{IDDES}}^2), 1.0] \tag{2.8}$$

$$\alpha_{IDDES} = 0.25 - \frac{d_{wall}}{\Delta} \tag{2.9}$$

where d_{wall} represents the shortest distance from the specified cell to the nearest wall, and Δ represents the grid spacing. The value of the blending function lies between 0 and 1, where 0 indicates that the corresponding cell is LES-dominant and 1 represents unsteady RANS-dominant.

In this research project, IDDES with *k*-ω SST model will be used to simulate the turbulent flow around a wall-mounted square cylinder. IDDES is chosen over the RANS models because:

1. The details of turbulence quantities such as velocity fluctuations are important for analyzing the flow field structures;
2. Strong separations are expected, which is a known weakness of any RANS model.

As expected, a well-setup LES model is known to have better performance than an IDDES model. Saeedi and Wang [21] conducted an LES study of flow past a wall-mounted finite square cylinder with AR = 4. A small computational domain was used in their study and the domain was meshed with 14.3 million computational cells. This reflects that very small grid spacing was applied in the domain to satisfy the mesh restrictions imposed by LES. Consequently, in order to keep a relatively safe Courant-Friedrichs-Lewy number (generally smaller than 1), the time step size had to be reduced, which means a very long period of time is required to complete the simulation. Their LES results will be used to compare with the current IDDES results in order to show that

adequate accuracy has been obtained with the IDDES model, while maintaining a higher computational efficiency than the LES model.

Chapter 3 Numerical Setup

3.1 Introduction

The computational domain for any simulation should be chosen with care. The boundaries of the domain should be placed adequately far from the cylinder in order to eliminate the influence from the boundaries, but not so far away as to incur the unnecessary additional computational expense. Although COST [22] provides good standards for this setup, the process of selecting an appropriate computational domain requires experience and testing. This chapter presents the computational domain and boundary conditions used in this investigation, along with the meshing methods and the grid independence study. At the end of this chapter, the computational model is validated against the experimental results of Bourgeois et al. [9] and El Hassan et al. [2].

3.2 Computation Domain

Based on the experimental work of El Hassan et al. [2] and Bourgeois et al. [9], a wall-mounted finite square cylinder with a width of d = 0.0127 m is selected for this study. The air flow has Reynolds number of 12,000 based on the freestream velocity (U_0) of 15 m/s and the cylinder width, with freestream turbulence intensity of 0.8% and dynamic viscosity of 1.855 x 10^{-5}Pa-s. The current study focuses on square cylinders with AR = 1, 2 and 4 immersed in the flow field with the above properties.

Figure 3.1 shows a schematic of the computation domain. In this study, the origin of the coordinate system is taken at the centre of the square cylinder at the bed level. The

x-, y- and z-coordinate directions correspond to the streamwise, spanwise and vertical directions, respectively. The inlet boundary is placed 6d upstream before the cylinder's windward surface (i.e. at x = -6.5d). Upstream distances of 10d and 20d have also been tested, where no significant influence on the flow field was found. The two slip walls on the side are placed 15d away (i.e. at y = ±15.5d) from each side-face of the cylinder, maintaining a blockage ratio of 3%. The outlet boundary is placed 40d downstream (i.e. at x/d = 40.5) of the cylinder's leeward surface to ensure elimination of reverse pressure gradients on the outlet boundary. The height of the domain is 11d, in order to ensure there is an adequate distance from the free-end shear layer of the AR = 4 cylinder, so that the streamwise velocity measured at the top wall is the same as the freestream velocity in the experiment.

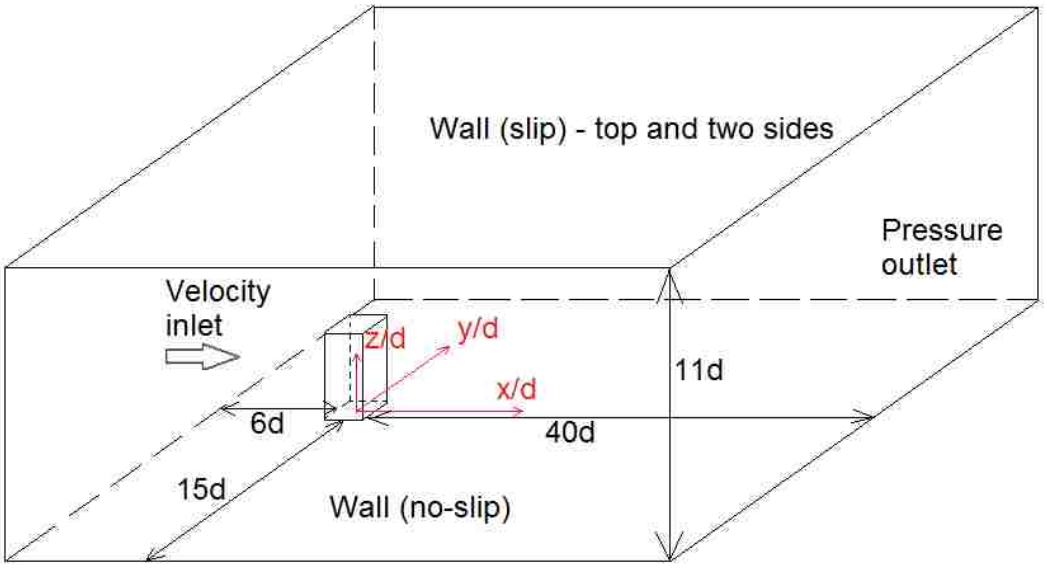

Figure 3.1 Schematic of the computation domain

3.3 Boundary Conditions

The side and top walls of the computational domain are smooth slip walls (Neumann boundary condition), and the bed and cylinder surfaces are smooth non-slip

walls (Dirichlet boundary condition). The outlet boundary is specified as a pressure outlet (Neumann boundary condition), and the static pressure in each outlet cell is set at 0 Pa.

The inlet condition has to be carefully assigned to match the flow field in El Hassan et al.'s experiment [2]. Figure 3.2 shows the boundary layer profile of the streamwise velocity ($U^+ = \overline{U}/u_\tau$) and the turbulence intensity ($\sqrt{\overline{u^2}}/U_0$) versus $Z^+ = \frac{z*u_\tau}{\upsilon}$ at the cylinder's location for the flow along a flat plate without the cylinder, where u_τ and υ represent friction velocity and kinematic viscosity, respectively. According to El Hassan et al. [2] and Bourgeois et al. [9], the boundary layer thickness (δ = 9.11 mm) at this location is 72% of the cylinder width.

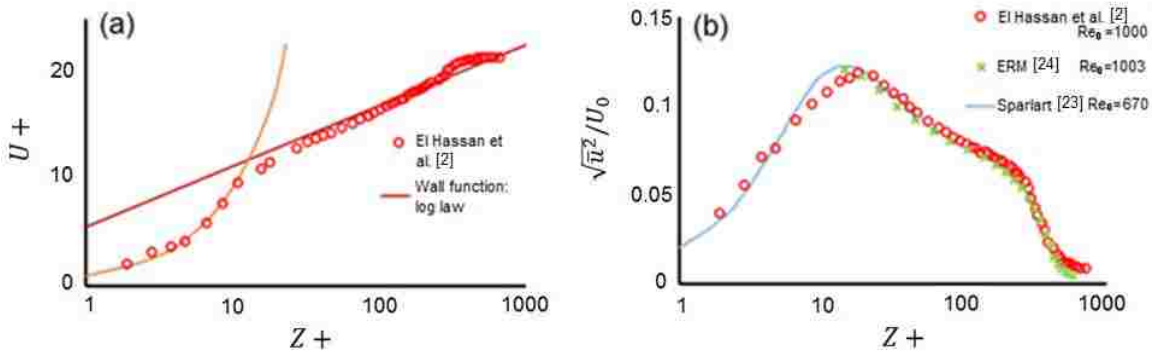

Figure 3.2 Experimental results [2] compared to wall function, DNS predictions [23] and other experimental results [24]; (a) time-averaged streamwise velocity, and (b) turbulence intensity

The two experimental profiles above demonstrate good agreement with the result of an Improved Delayed Detached Eddy Simulation (IDDES) study of flow along a flat plate [23] as well as the log law of the wall. However, simulations using the currently available standard RANS models show that the turbulence intensity profiles are poorly matched at this Re_θ value ($Re_\theta = \delta * U_0/\upsilon \approx 1000$), as seen in Fig. 3.3. The peak turbulence intensity value in the boundary layer is only half of the experimental value.

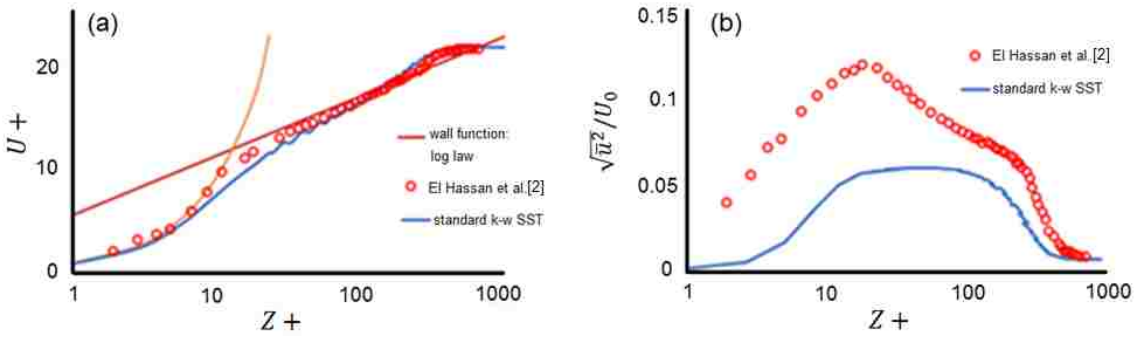

Figure 3.3 Comparison between k-ω SST predictions, at the cylinder location with the cylinder removed, and the experimental results by El Hassan et al. [2]; (a) time-averaged streamwise velocity, and (b) turbulence intensity

In a standard *k-ω* model, the turbulence kinetic energy (*k*) is quickly diffused in the near-wall region by an excessively large value of specific turbulence dissipation rate (ω) [17]. This formulation is valid when Re_θ (based on the boundary layer thickness) is significantly greater than 10,000. When Re_θ is relatively small, the turbulence dissipation rate ω tends to damp out an extra amount of turbulence kinetic energy and leads to the under-prediction of turbulence intensity by the Boussinesq approximation, as seen from the expression

$$T.I. = \sqrt{\overline{u^2}}/U_0 = \sqrt{\frac{2}{3}k} \tag{3.1}$$

To overcome the deficiency of the model for low Re_θ, Wilcox [17] modified the *k-ω* model with three extra variables: R_β, R_ω, and R_k. These variables are designed to help restrict the value of specific dissipation rate at the wall while not disturbing the main flow field. The governing equations for *k* and ω are modified to:

$$\bar{U}\frac{\partial k}{\partial x} + \bar{V}\frac{\partial k}{\partial y} = v_T\left(\frac{\partial \bar{U}}{\partial x}\right)^2 - \beta^*\omega k + \frac{\partial}{\partial y}\left[(v + \sigma^* v_T)\frac{\partial k}{\partial y}\right] \tag{3.3}$$

$$\bar{U}\frac{\partial \omega}{\partial x} + \bar{V}\frac{\partial \omega}{\partial y} = \alpha\frac{\omega}{k}v_T\left(\frac{\partial \bar{U}}{\partial x}\right)^2 - \beta\omega^2 + \frac{\partial}{\partial x}\left[(v + \sigma\mu_T)\frac{\partial \omega}{\partial x}\right] \tag{3.4}$$

where $\alpha^*, \alpha, \beta^*$ are defined as:

$$\alpha^* = \frac{\alpha_0^* + Re_T/R_k}{1 + Re_T/R_k} \tag{3.5}$$

$$\alpha = \frac{5}{9}\frac{\alpha_0 + \frac{Re_T}{R_\omega}}{1 + \frac{Re_T}{R_\omega}}(\alpha^*)^{-1} \tag{3.6}$$

$$\beta^* = \frac{9}{100}\frac{\frac{5}{18} + (\frac{Re_T}{R_\beta})^4}{1 + (\frac{Re_T}{R_\beta})^4} \tag{3.7}$$

where the values of the constants are:

$$\beta = \frac{3}{40}, \sigma = \sigma^* = \frac{1}{2}, \alpha_0^* = \frac{1}{40}, \alpha_0 = \frac{1}{10}$$

The turbulent Reynolds number Re_T in these equations is defined as:

$$Re_T = \frac{k}{\omega \upsilon} \tag{3.8}$$

From testing, the optimized values of R_β, R_ω and R_k are:

R_β	30
R_k	12
R_ω	2.95

With the optimized values of R_β, R_ω and R_k, the *k*-ω model with low-Reynolds number modification is capable of predicting the streamwise velocity and turbulence intensity with sufficient accuracy as shown in Fig. 3.4, although the peak value of turbulence intensity is still under-predicted by about 15%. By raising the value of R_β to 40, the turbulence intensity profile will get closer to that of the experiment, but the

velocity profile will be heavily affected. Although it is possible to determine the best set of values by trial and error, a compromise has to be made because the major influence to the flow is the bluff body, not the turbulence intensity profile of the boundary layer.

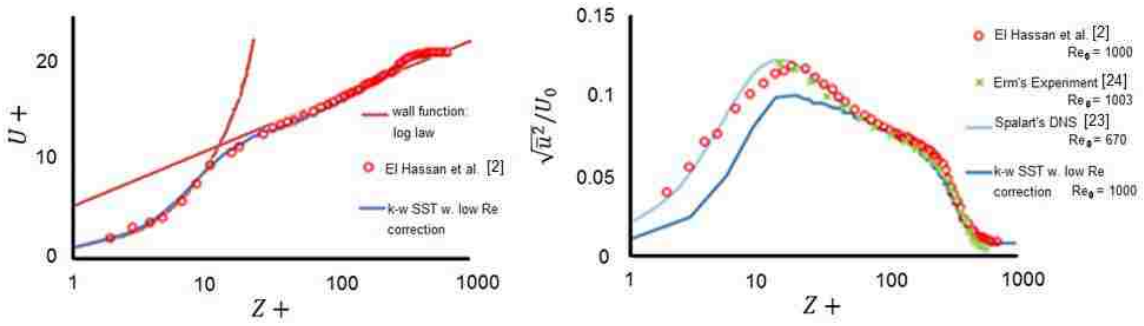

Figure 3.4 Streamwise velocity (left) and turbulence intensity (right) profiles plotted at the cylinder's location, with the cylinder removed.

The streamwise velocity (U), turbulence kinetic energy (k) and specific turbulence dissipation rate (ω) profiles are taken at the location 6.5d upstream of the cylinder and mapped onto the inlet boundary of the computational domain. This ensures that the flow has the same characteristics as the experiment at the cylinder's location.

3.4 Grid

A polyhedral, unstructured, surface-controlled mesh is used for this study. Our tests have shown that the polyhedral unstructured mesh allows better clustering at the cylinder corners and proper transition from the prism layers near the surfaces. The surface-controlled mesh yields results that are closer to the experiment than the results from a volume-controlled mesh. The grid spacing is defined on the cylinder surface and the bed. Ten prism layers are placed on the no-slip walls with adequate spacing to ensure more than five cells lie inside of the viscous sub-layer. The polyhedral cells in the rest of the

computational domain have a slow growth rate outward from the wall. Figure 3.5 shows the centre plane of the AR= 4 cylinder with the surface cell size of 1 mm.

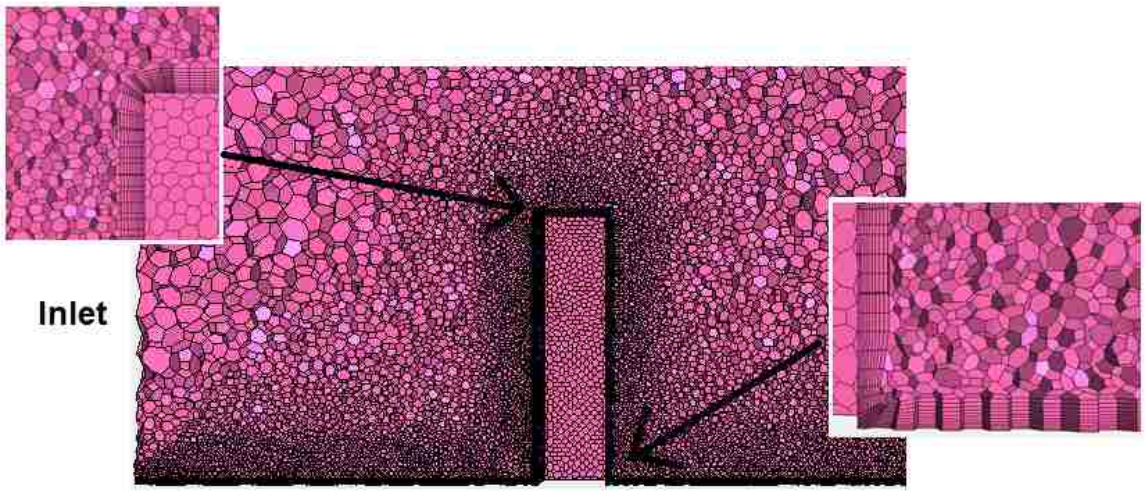

Figure 3.5 Illustration of the polyhedral grid on the central plane

A study of grid independence provides information on the optimal cell size relative to computational accuracy. Since DES uses an implicit time-marching scheme, the Courant-Freidrichs-Lewy (CFL) number may exceed 1 as long as the residuals of the governing equations converge to zero. Table 3.1 presents the parameters used for each mesh tested in this study. Meshes 1, 2 and 3-a represent coarse, finer and finest mesh respectively, with the same time step size of 2 x 10^{-4} s. Mesh 3-b was also used with the time step size at 1 x 10^{-4} s to understand the effect of CFL number on the result.

Table 3.1 Grid independence study for AR = 4, with exponentially decaying cell size and two time step sizes

	cell size (mm)	time step size (ms)	CFL Number	Cell count	Legend
Mesh 1	2	0.2	1.5	4M	
Mesh 2	1	0.2	3	5.6M	
Mesh 3-a	0.5	0.2	6	7.8M	
Mesh 3-b	0.5	0.1	3	7.8M	
Bourgeois et al. [9]	-	-	-	-	O

Figs. 3.6(a) and (b) show profiles on the middle plane behind the AR = 4 cylinder at different elevations. The profiles of Mesh 1 at all levels are significantly off from other schemes. Mesh 2 is slightly different from Mesh 3-a, Mesh 3-b, and the experimental result between x/d = 0.5 and x/d = 4, which encompasses the wake region. Reducing the grid spacing from 1 mm to 0.5 mm on the cylinder's faces provides a subtle improvement. However, the effect of time step size is almost negligible because the velocity profiles of Mesh 3-a and Mesh 3-b are very close to each other.

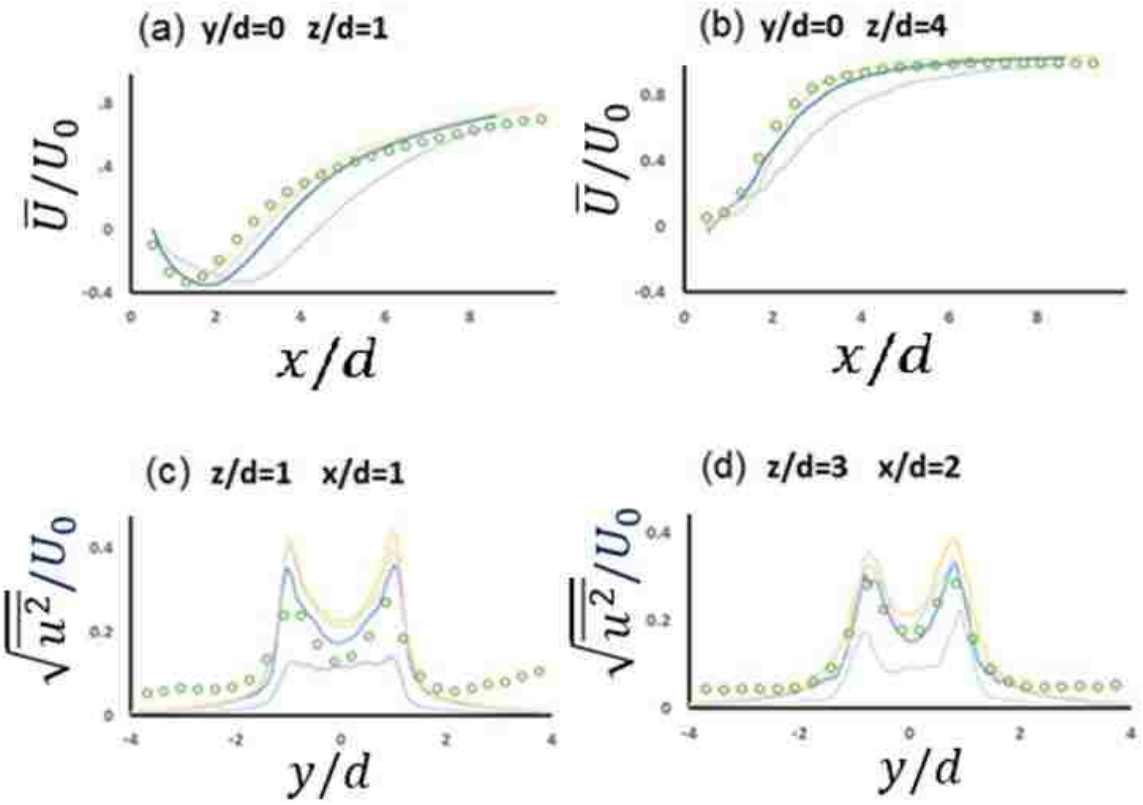

Figure 3.6 Comparison of the time-averaged streamwise velocity ($\overline{U}/U_0$) and turbulence intensity ($\sqrt{\overline{u^2}}/U_0$) with different meshes and experimental result

In the horizontal planes, almost all mesh schemes predicted the mean velocity in x- and y-direction. The main difference between each mesh lies in the turbulence

quantities: in Figs. 3.6 (c) and (d), $\sqrt{\overline{u^2}}/U_0$ was slightly over-predicted by Mesh 2, 3-a and 3-b. It is difficult to distinguish which one amongst Mesh 2, 3-a, and 3-b is significantly better, but all closely represents the result from Bourgeois et al.'s experiment [9].

In conclusion, Mesh 1 is too coarse to produce a reliable and accurate result. The results from Meshes 2, 3-a and 3-b are closer to the experimental values measured by Bourgeois et al. [9]. Since Mesh 2 is more computationally efficient than Mesh 3-a and 3-b due to the reduction in cell count, cylinders with AR = 2 and 4 use Mesh 2. To increase the number of cells on the side wall of the cylinder which is smaller in size, the cylinder with AR = 1 uses Mesh 3-a. Mesh 3-b does not show any superiority over other mesh schemes, and it almost doubles the computational time over that of Mesh 3-a.

3.5 Validation

The experimental study of Bourgeois et al. [9] served as a benchmark in a challenge problem at the CFD Society of Canada Annual Conference in 2012. Subsequently, Bourgeois et al. [24] and El Hassan et al. [2] compiled the results and conducted further studies on the flow field around the cylinder with AR = 4. The same problem was also studied by Saeedi and Wang [21] with LES and by Saeedi et al. [26] using DNS. The experimental results from the study by Bourgeois et al. [9] and the LES results by Saeedi and Wang [21] were used to validate the current DES results.

Fig. 3.7 shows the streamtraces on the centre plane y/d = 0 shaded by the streamwise velocity contour, with the DES simulation result on the left and the experimental result on the right. On the windward surface of the cylinder, the stagnation

point in both figures is located at the same level (z/d ≈ 2). Flow above the stagnation point moves upward and reaches the leading edge of the free-end. Behind the cylinder, the flow moves sharply downward around x/d = 3 and recirculates to the leeward side of the cylinder at z/d = 1. An upwash flow structure beneath the recirculation bubble is observed at x/d ≈ 3 in both figures.

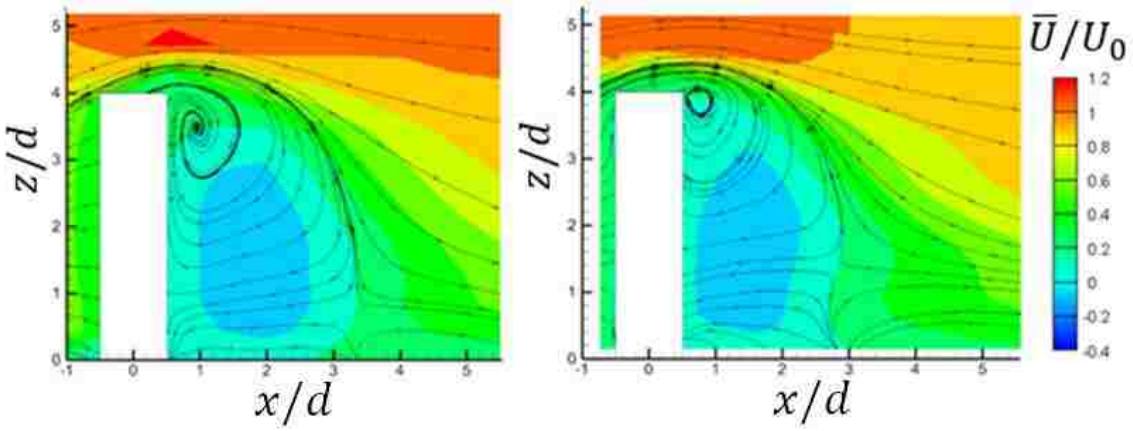

Figure 3.7 Validation of the current DES result (left) against the experimental result (right) by Bourgeois et al. [9] at the centre plane y/d = 0

The time-averaged normalized streamwise velocity $\bar{U}/U_0$ was tracked behind the body on the middle plane at the levels of z/d = 2 and z/d = 3 as shown in Fig. 3.8. The DES results show good agreement with Bourgeois et al.'s experimental results [9]. At both levels, $\bar{U}/U_0$ has zero value on the wall and then becomes negative due to the reverse flow from the recirculation. After x/d ≈ 3, $\bar{U}/U_0$ becomes positive again and slowly recovers to the freestream velocity of the incoming flow approximately at x/d ≈ 9.

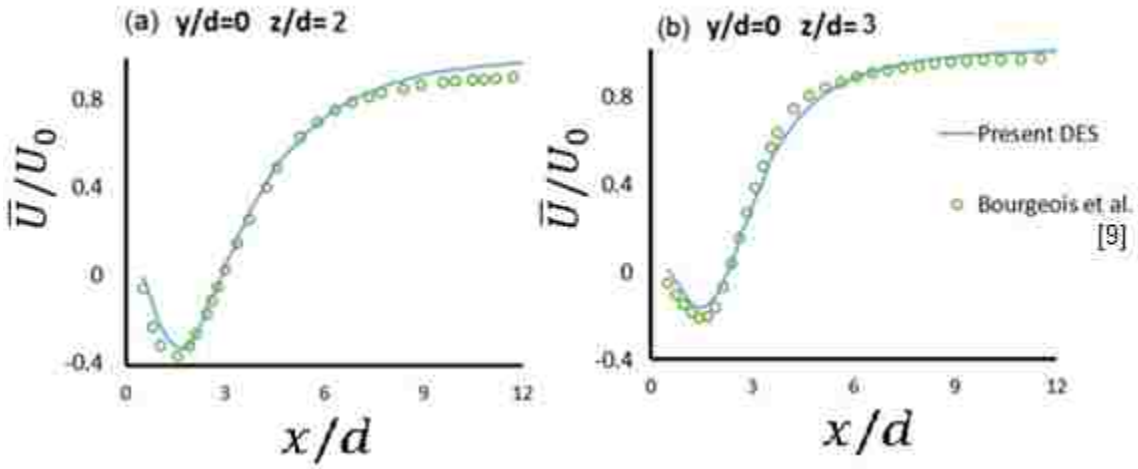

Figure 3.8 Time-averaged normalized streamwise velocity ($\overline{U}/U_0$) on y/d = 0 plane, behind the cylinder at the vertical level of (a) z/d = 2 and (b) z/d = 3.

On the horizontal plane z/d = 3, time-averaged normalized streamwise and spanwise velocity ($\overline{U}/U_0$ and $\overline{V}/U_0$) and root-mean-square of the fluctuation of the streamwise and spanwise velocity ($\sqrt{\overline{u^2}}/U_0$ and $\sqrt{\overline{v^2}}/U_0$) are tracked at the location of x/d = 2. Fig. 3.9 compares the results from the current DES study with the experimental results, as well as the LES results by Saeedi and Wang [21].

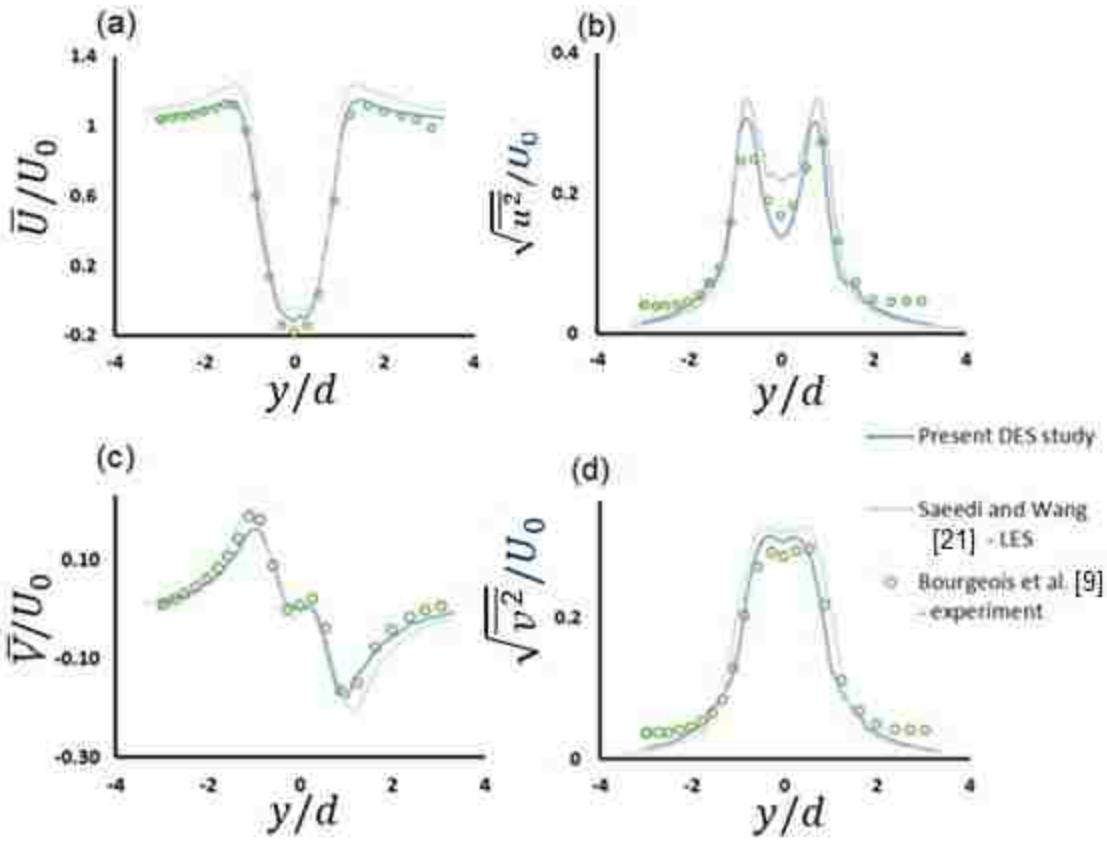

Figure 3.9 Validation of the current DES model with experimental result and an LES study on the plane z/d = 3 at the location x/d = 2: (a) time-averaged streamwise velocity ($\overline{U}/U_0$) and (b) fluctuating streamwise velocity root-mean-square($\sqrt{\overline{u^2}}/U_0$); (c) time-averaged spanwise velocity ($\overline{V}/U_0$); (d) fluctuating spanwise velocity root-mean-square ($\sqrt{\overline{v^2}}/U_0$)

The current DES study shows good agreement with the experimental streamwise and spanwise velocity profiles. At the two ends of the profiles, the values of normalized streamwise velocity become very close to unity. The lowest streamwise velocity inside the wake region is located at y/d = 0. At the location of x/d = 2, both DES and LES slightly under-predict the peak streamwise velocity. This feature is also shown on the central plane (Fig. 3.7) as a slightly extended recirculation zone in Bourgeois et al.'s [9] experiment velocity contour. The fluctuation of streamwise and spanwise velocities ($\sqrt{\overline{u^2}}/U_0$ and $\sqrt{\overline{v^2}}/U_0$) slightly mismatch the corresponding experimental profiles.

Overall, the mismatch is considerably low compared with the LES solution. Thus, the current DES model has been validated and is regarded as capable of predicting the size and strength of the separation and the recirculation zone.

Chapter 4 Results and Discussion

4.1 General Remarks

In this chapter, the time-averaged and the instantaneous flow field characteristics are discussed. As the fluid negotiates around the wall-mounted cylinder, it experiences separation from three edges, the formation of the horseshoe vortex near the bed in front of the body and formation of a wake region behind the cylinder. However, the effect of the flow separating from the top edge of the cylinder and the effect of the bed on the wake characteristics can vary depending on the aspect ratio. The characteristics of interest include the dominant shedding frequency of the wake vortices, the pressure distribution on the body, and the mean and instantaneous velocity field in the wake. The flow field is also visualized using the λ_2 criterion to develop an overall picture of the wake structure. These aspects are discussed in this chapter.

4.2 Vortex Shedding Frequency

In the simulation, probes were placed in the wake region behind the cylinder for the purpose of tracking the spanwise velocity. Using this velocity time history, the power spectral density was calculated, and a sample is illustrated in Fig. 4.1. The dominant peak corresponding to the vortex shedding frequency (~120 Hz) was found to be the same for all three values of AR. The corresponding Strouhal number (St = fd/U_0) is calculated to be 0.103, which matches well with the 0.104 obtained by El Hassan et al. [2] for AR = 4. This serves as an additional validation of the simulation results. The value of St is lower than that measured in the flow past an infinitely long square cylinder, which is in the range 0.125 to 0.130 [27]. However, Zdravkovich [28] observed that the downwash flow from the free-end of a wall-mounted finite cylinder extends the region of vortex

formation and widens the wake, which consequently reduces the frequency of vortex shedding. A similar effect has been recorded by other experimental researchers, e.g. [4]. The fact that the Strouhal number does not change with cylinder height is an indication that the aspect ratio has little effect on the vortex shedding characteristics.

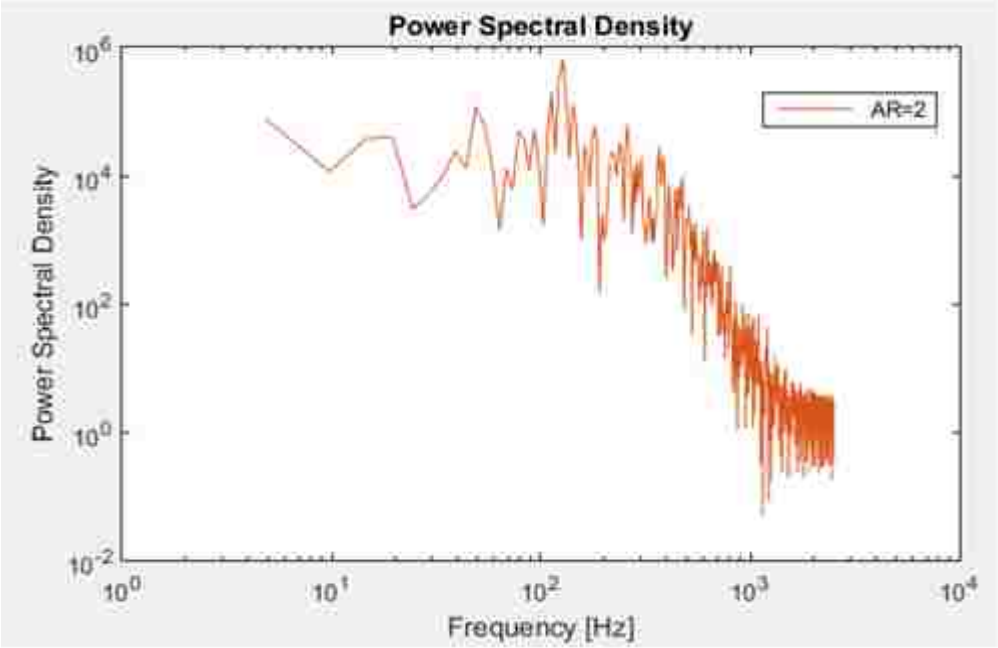

Figure 4.1 Power spectral density for AR = 2

4.3 Time-averaged Velocity Field

To ensure that the flow field has statistically achieved a steady state, the time averaging of the velocity data was commenced after 100 cycles of vortex shedding. The time-averaged results from over 60 vortex shedding cycles was calculated and is presented in the following sections.

4.3.1 Velocity Field in Central Planes and Side Faces

The time-averaged streamwise velocity contours, with superimposed streamtraces, on the central plane (y/d = 0) and the side-face plane (y/d = 0.5) of each cylinder are shown in Fig. 4.2. There are obvious similarities in the contours shared by the three

aspect ratios: the presence of the horseshoe vortex (HSV), the formation of the separating streamline at the top edge followed by the downward flow into the wake region and the formation of the recirculation region immediately behind the body.

As the incoming flow impinges on the windward face of each cylinder, the flow splits and a portion of the fluid moves upwards and over the free-end. There is also a significant amount of the approach flow which moves downwards and rolls up into a horseshoe vortex close to the bed. The horseshoe vortex can also be seen on the side-face plane, but the vortex is somewhat reduced in size in Figs. 4.2(d), (e) and (f) as the horseshoe vortex tube turns from the spanwise direction towards the streamwise direction as it moves downstream.

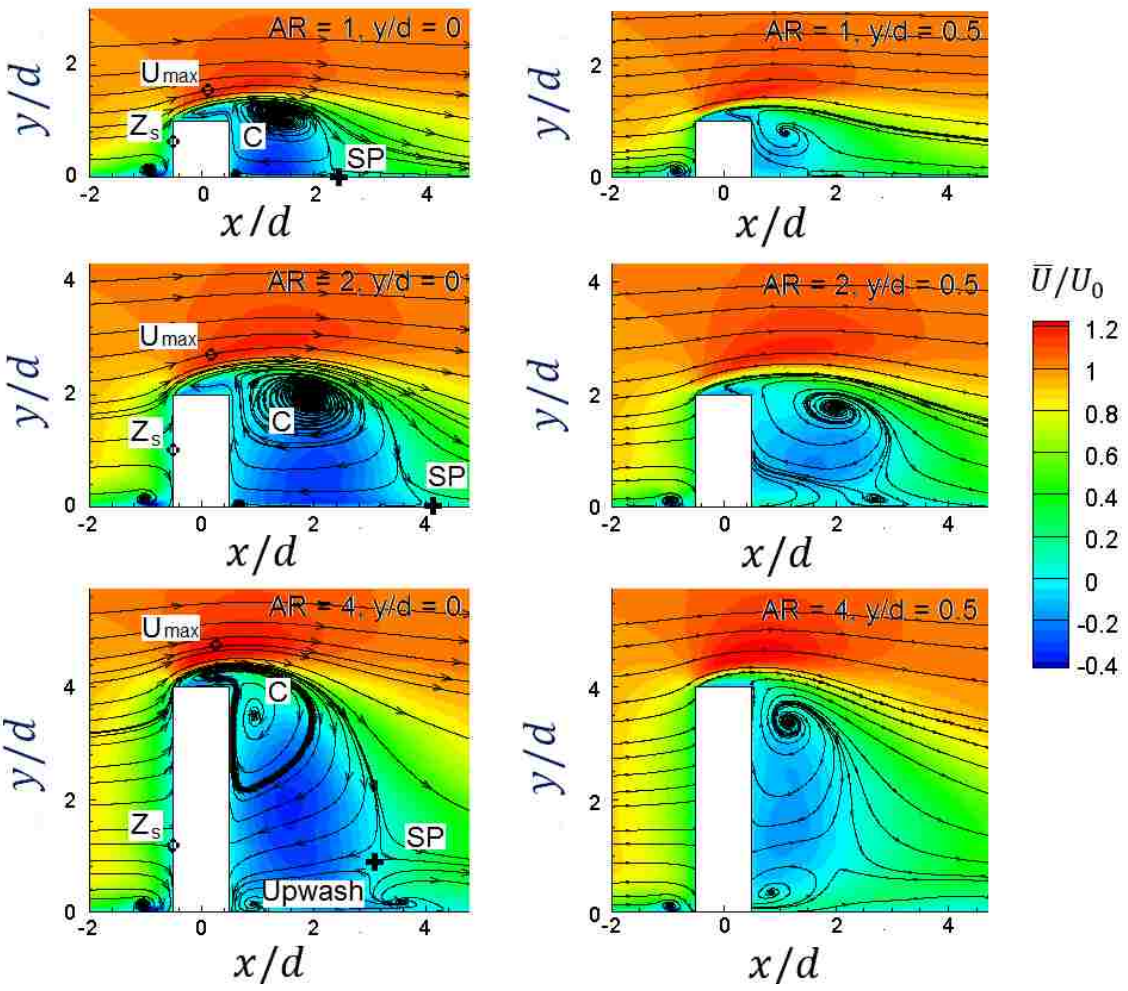

Figure 4.2 Time-averaged normalized streamwise velocity ($\overline{U}/U_0$) contours on central plane (y/d = 0) for (a) AR = 1, (b) AR = 2, (c) AR = 4; and on side-face plane (y/d = 0.5) for (d) AR = 1, (e) AR = 2, (f) AR = 4.

At the cylinder's free-end, due to flow separation, a shear layer is formed. The magnitude of the local peak velocity (U_{max}/U_0) in this region increases as the cylinder AR increases, albeit slightly, due to the increasing pressure difference between the windward and leeward faces. The location of the peak velocity moves further away from the free-end of each cylinder in the downstream and normal directions as the cylinder AR increases, as shown in Table 4.1.

Table 4.1 Magnitudes and coordinates of U_{max}

AR	U_{max}/U_0	x/d	(z - h)/d
1	1.18	0.013	0.41
2	1.20	0.060	0.55
4	1.27	0.113	0.57

As noticed in Fig. 4.2, the downwash flow creates a recirculation in the wake region close to the top edge of the body. The core of the recirculation is marked by "C" in Figs. 4.2 (a), (b) and (c). The size and location of the recirculation induced by the downwash flow vary with AR. Table 4.2 lists the coordinates of the vortex core in each case, where the values of the streamwise and normal velocity are found to be zero, and the local pressure is found to be a minimum.

Table 4.2 Coordinates of the vortex cores (marked as C in Figs. 4.2 (a), (b) and (c)).The experimental result [3] for AR = 7 is indicated with an asterisk)

AR	x/d	z/d	z/h
1	1.26	1.16	1.16
2	1.73	1.93	0.97
4	0.99	3.49	0.87
7*	1.07*	6.79*	0.97*

A saddle point (indicated by SP) occurs in the flow as shown in Fig. 4.3 (extracted from [3]) for AR = 7. This figure confirms the pattern of both the recirculation zone and the variation of the location of the saddle point with AR noticed in the present study. The streamwise location of a saddle point in the wake indicates whether the flow tends to move towards the body or outwards in the streamwise direction, while the vertical location of the saddle point indicates the location where the downward-moving flow and the upward-moving flow meet. In Figs. 4.2(a, b), the saddle point is not clearly identifiable and is located on the bed for cylinders with AR = 1 and 2, which shows that the upward moving flow does not exist.

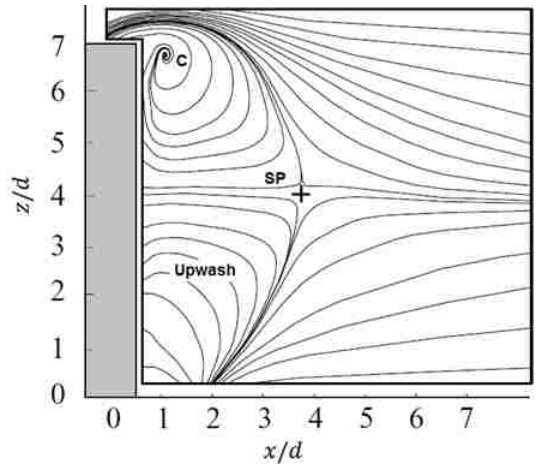

Figure 4.3 Time-averaged streamtraces for flow past a cylinder with AR = 7, (from Wang and Zhou [3])

Table 4.3 Coordinates of the saddle points

AR	x/d	z/d	(h-z)/d
1	2.20	0.00	1.00
2	3.40	0.00	2.00
4	3.22	0.91	3.09
7*	3.70*	4.03*	2.97*

As the cylinder AR is increased from 1 to 2, the value of U_{max} increases as shown in Table 4.1. This causes the separating streamline to travel farther away from the body. The streamline eventually turns and impinges on the bed forming the recirculation region, which causes the vortex core and the saddle point to move farther downstream from x/d = 1.26 to x/d = 1.73, and from x/d = 2.2 to x/d = 3.4, respectively. However, when AR = 4, as indicated by the location of the U_{max} in Table 4.1, the streamline initially travels upwards and then quickly turns towards the bed. This causes the vortex core to move closer to the body (x/d = 1) and the recirculation region to become slightly smaller than that noticed in the AR = 2 case. Correspondingly, the streamwise location of the saddle point moves slightly towards the cylinder at x/d ≈ 3. As the cylinder AR is further increased to 7 [3], the streamwise location of the saddle point remains roughly at the same location as observed for AR = 4. The vertical distance between the saddle point and

the top edge of the cylinder remains the same as well. This further indicates that the size of the recirculation region is not significantly influenced by the cylinder AR when AR is increased above a value of 4.

The downwash flow due to the presence of the cylinder free-end restrains the upward motion of the flow from the bed. As the cylinder AR increases to 4 in Fig 4.2 (c), the downwash flow is not strong enough to dominate the entire wake due to the increasing distance between the free-end and the bed. Therefore, a flow structure with an upward movement, commonly designated by researchers as upwash (Sumner [4], Bourgeois et al. [9]), appears in the near-bed wake region. The upwash flow structure can also be observed Fig.4.3 from the study of Wang and Zhou [3] at AR = 7. The upwash structure presented by Wang and Zhou [3] has its origin close to the leeward face of the cylinder at approximately x/d = 2, as opposed to at x/d = 3.5 for AR = 4 in the present study. The shape of the upwash structure at AR = 7 is similar to the upwash structure in the flow field of an emergent body with AR = 11 as shown in Fig. 4.4 [29]. By comparing the upwash structure of AR = 4 with the upwash of taller bodies, it is obvious that the upwash flow for AR = 4 is not fully evolved due to the influence of the downwash.

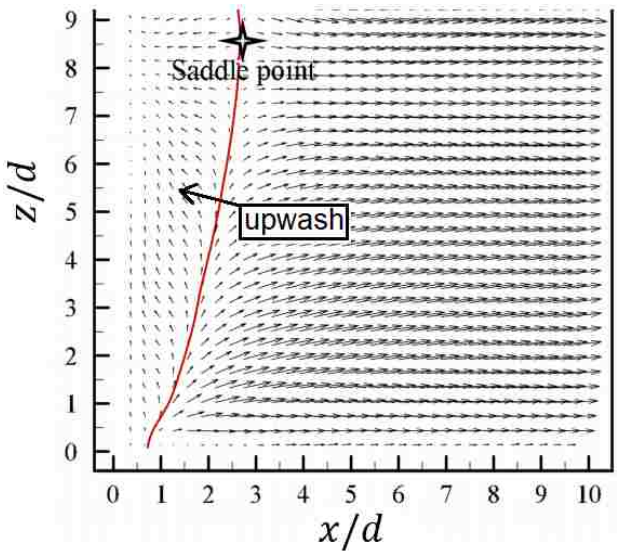

Figure 4.4 Time-averaged velocity vectors for flow past an immersed circular cylinder, (from Heidari [29])

Fig. 4.5 presents the streamtraces of the recirculation near the free-end of the body for AR = 1 (a and d), AR = 2 (b and e), and AR = 4 (c and f) on central planes (a, b and c) and side-face planes (d, e and f). By closely examining the recirculation in the central plane and the side-face plane for each case, a change in flow pattern can be found when the cylinder AR is increased from 2 to 4. As noted by Perry and Fairlie [30], an inward-spiral vortex commonly termed as a stable focus is seen in Fig. 4.5(c). An outward-spiral vortex, termed as an unstable focus, is noticed in Fig. 4.5(d). In the central plane of the cylinder with AR = 1 and 2, both recirculation vortices are identified as unstable foci. They are consistent with the recirculation found in their respective side-face planes. However, the recirculation of the cylinder with AR = 4 is presented as a stable vortex in the central plane but as unstable in the side-face plane. Fig. 4.6 presents sections of the recirculation in the case of AR = 4 from the central plane (y/d = 0) to the plane that is 0.3d beyond the side-face plane. The cross-section of the recirculation from y/d = 0 to y/d = 0.3 shown in Figs. 4.6(a) to (d) are similar in size and are all inward-

spiraling. As the field-of-view is translated from y/d = 0 to y/d = 0.3, the streamtraces are found to be denser, which means an arbitrary fluid particle along the streamtrace takes a longer route to enter the vortex core from the outer region. From y/d = 0.4 to y/d = 0.6 shown in Figs. 4.6(e) to (g), the cross-sections of the recirculation is outward-spiraling. Also, the streamtraces become less dense as the field-of-view moves away from the central plane, which is different from the observations on the planes from y/d = 0 to y/d = 0.3. For y/d > 0.6, the recirculation can no longer be captured as in Figs. 4.7(h) and (i). The inward-spiraling vortex is considered stable since it experiences an axial expansion strain, which amplifies its vorticity. The outward-spiraling vortex experiences an axial compression strain, which tends to buckle the vortex filament.

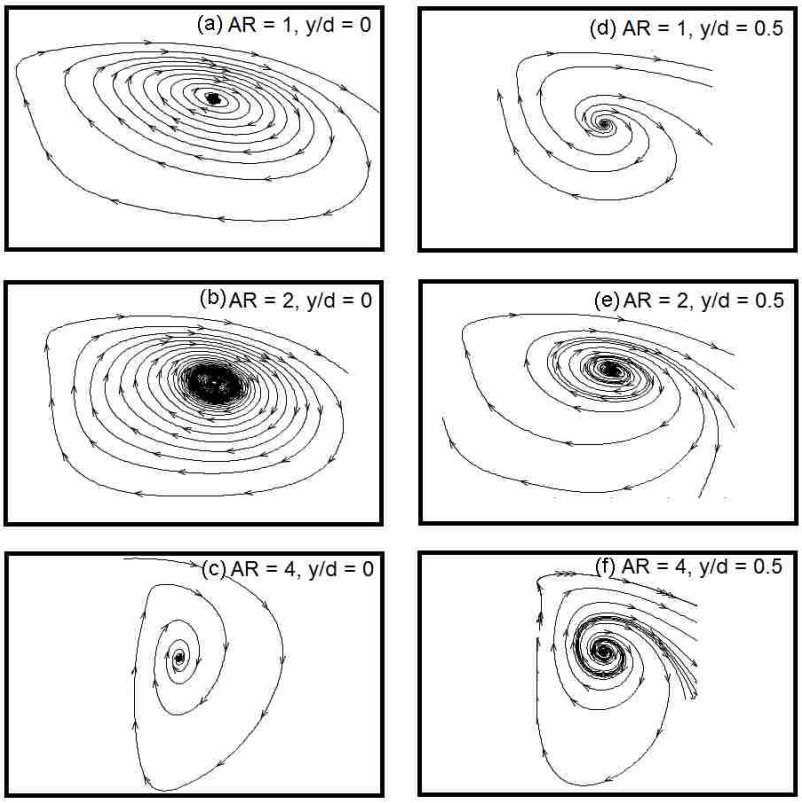

Figure 4.5 Time-averaged streamtraces of the recirculation in the flow field for (top row) AR = 1, (middle row) AR = 2, (bottom row) AR = 4 on their central planes (left column) and side-face planes (right column)

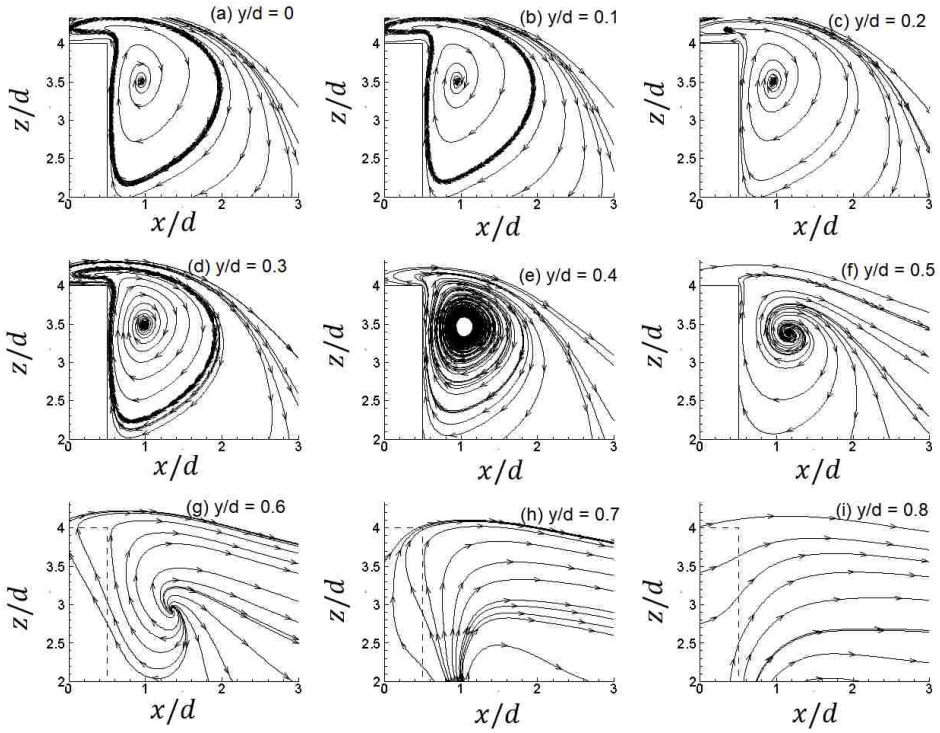

Figure 4.6 Time-averaged streamtraces for the recirculation in the flow field of AR = 4 in vertical planes (from y/d = 0 to 0.8)

Figs.4.7-4.11 show the streamtrace pattern in the transverse (y-z) planes for each AR from the location of the windward face of each cylinder (x/d = -0.5) to a downstream location (x/d = 1). The transverse planes at other locations were examined, but the ones that are presented in this section are the ones in which the streamtrace pattern shows important changes.

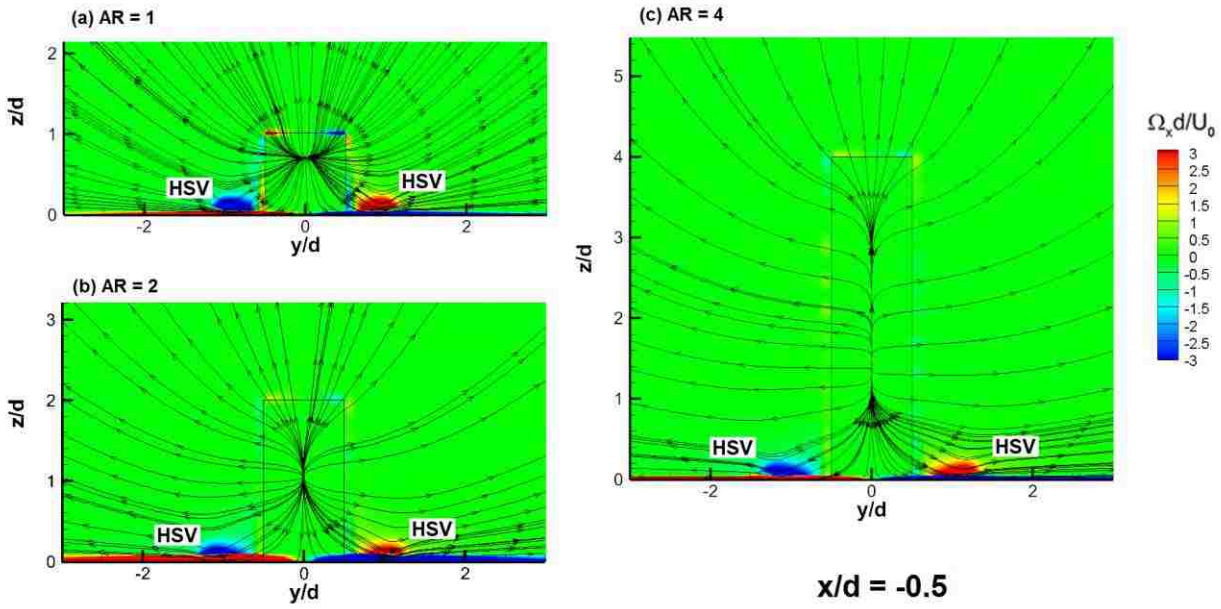

Figure 4.7 Streamtraces in the transverse plane at x/d = -0.5

Fig.4.7 shows the streamtrace pattern on the windward face of the body. The pattern for each AR on the transverse plane shows many similarities. At AR = 1, there is the presence of a horizontal line source around z/d = 0.7, while at the higher AR values there is a tendency to form a vertical line source. At the near-bed level, there is a significant curl in the streamtrace on each side of the cylinder at all three values of AR and represents the horseshoe vortex. As will be seen in the upcoming figures, this pair of streamtrace curls can also be found in other downstream planes as well.

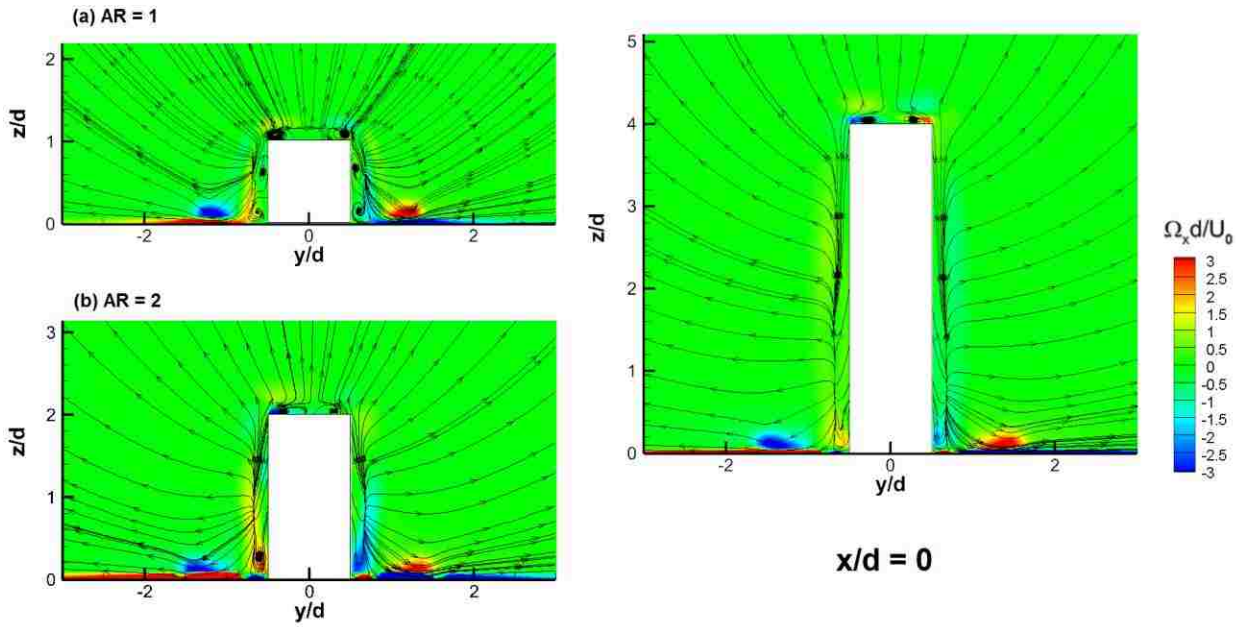

Figure 4.8 Streamtraces in the transverse plane at x/d = 0

In Fig.4.8, in the transverse plane through x/d = 0, three pairs of vortices are visible at AR = 1. There is one vortex pair on the top of the cylinder and two on the sides. At the cylinder's free-end, the pair of counter-rotating vortices are formed due to the corner effect. This pair of vortices can be observed clearly in the transverse plane at x/d = 0, and at subsequent downstream values of x/d. It starts diminishing after this location.

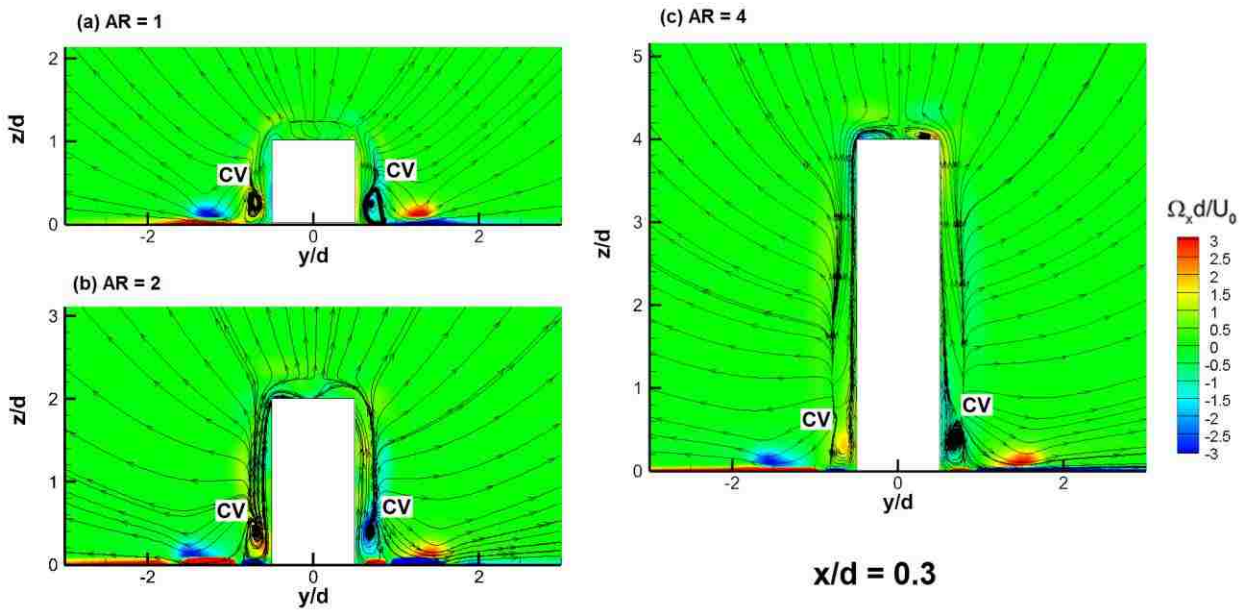

Figure 4.9 Streamtraces in the transverse plane at x/d = 0.3

In the plane through x/d = 0.3 (shown in Fig.4.9), just prior to the leeward face of the cylinder, the pair of vortices above the cylinder's free-end is barely visible at AR = 1. The mid-depth vortex noticed in the previous figure is absent at AR = 1. A pair of counter-rotating vortices can be found at the corner of side face of the cylinder and the bed (marked as CV). This pair of vortices is similar to collar vortex noted by Nasif et al. [13] in the flow past a sharp-edged bluff body.

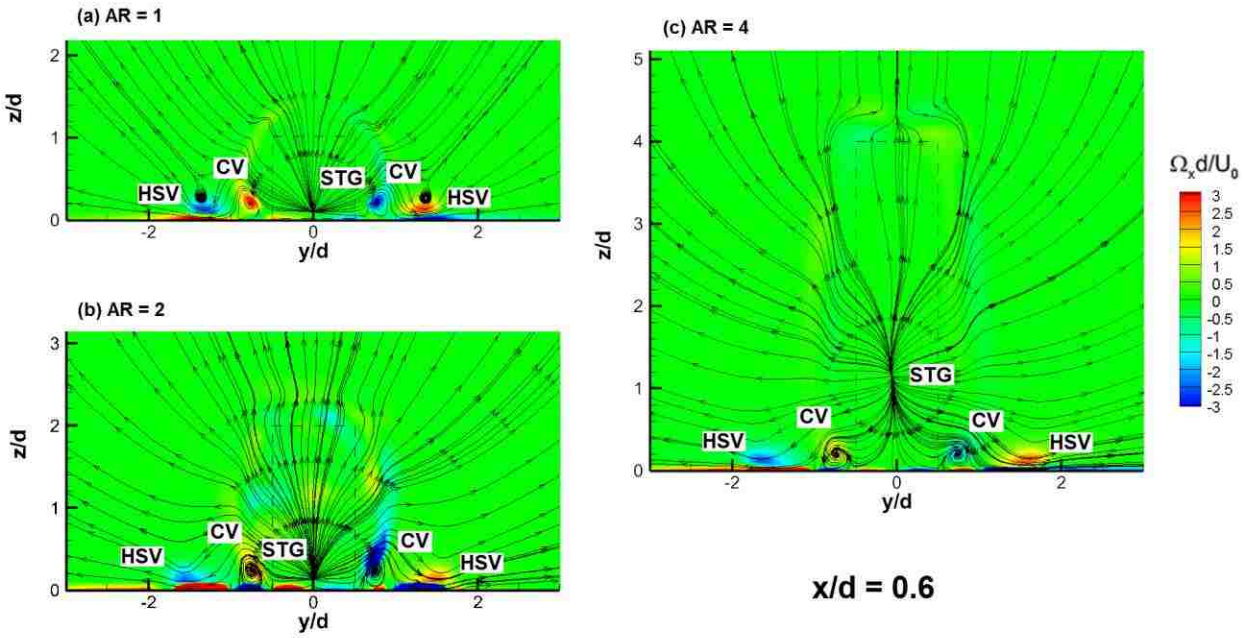

Figure 4.10 Streamtraces in the transverse plane at x/d = 0.6

Similar to the observation at x/d = 0.3, each flow field in Fig. 4 consists of horseshoe vortex and collar vortex in the near-bed region at x/d = 0.6. It can be noticed that a stagnation point (marked as STG) appears in each case on the leeward face of the cylinder. The stagnation point is located at the near-bed level for both AR = 1 and 2, and it moves to z/d = 1 as the cylinder AR is increased to four due to the presence of the upwash observed in the vertical plane (Fig.4.2 (c)). Above the stagnation point, the streamtraces show that the flow behind the cylinder tend to be towards the sides of the body for AR = 1 as shown in Fig.4.10 (a), due to the influence of the collar vortex and the horseshoe vortex (marked as CV and HSV in the figure). Fig.4.10 (b) shows the flow above the stagnation point is weakly influenced by the vortices on the sides of the cylinder for AR = 2. In the flow field for AR = 4, it can be observed that the flow above the stagnation point forms a bubble at the upper section (between z/d = 2 and 4.5) of the

wake. The flow leaves the center of the wake (y/d = 0) from both sides, then returns to the center at a level slightly above the cylinder's free-end.

In Fig.4.11 (a), a saddle point (SP) and nodal point (NP) located on each side of the cylinder can be observed in the transverse plance through x/d = 1. These points are not distinguishable at higher values of AR. Also, it can be noted that the horseshoe vortex becomes weaker as the cylinder AR increases (judging by the curvature of the streamline). The size of the horseshoe vortex is reduced as they move apart by increasing the cylinder AR. At AR = 4, two vortices located at z/d = 4 entrain fluid to the centre of the recirculation (y/d = 0). These two vortices have their cores located at y/d = 0.3 and -0.3, and this is the location where the transition from an inward to an outward spiraling vortex occurs in the vertical planes (x-z planes).

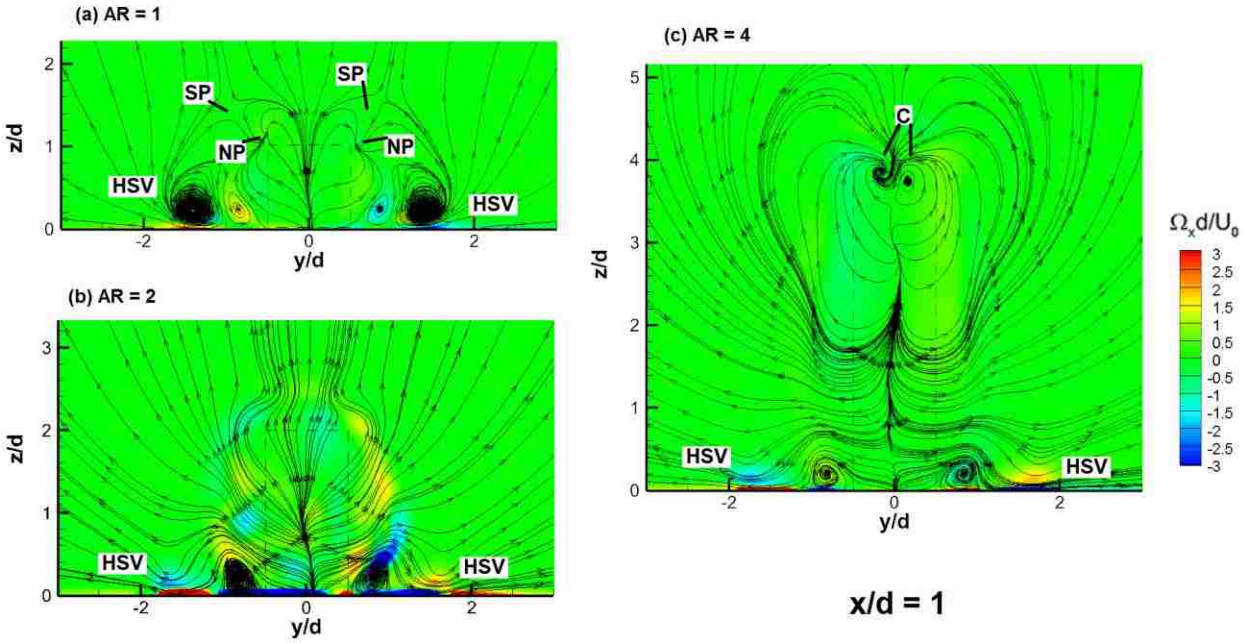

Figure 4.11 Streamtraces in the transverse plane at x/d = 1

4.3.2 Velocity Field on Horizontal Planes (Traditional Method)

Traditionally, when researchers select the location of the horizontal planes for the purpose of analyzing the wake flow, they chose the location based on the geometry of the flow field, such as height (Heidari et al. [29]), width (Vinuesa et al. [31]), or flow depth (Akilli and Rockwell [32]). In the present study, the only parameter that can be selected is the height, since all other parameters such as width and boundary layer thickness are held constant. For the three aspect ratios used in the present study, Figs. 4.7 and 4.8 show the normalized streamwise velocity ($\overline{U}/U_0$) and the normalized normal velocity ($\overline{W}/U_0$) distributions in three horizontal planes at locations relative to the cylinders height, i.e., z/h = 0.25, 0.5 and 0.75 in left, middle and right columns, respectively.

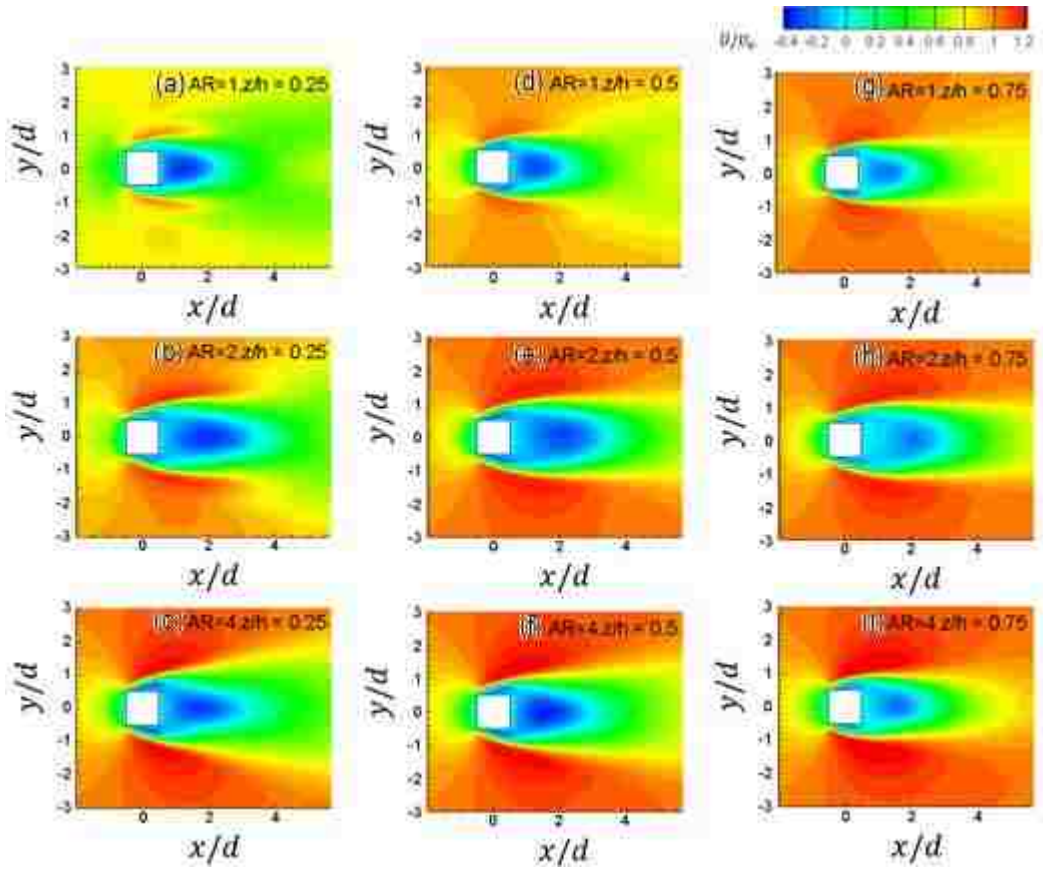

Figure 4.12 Horizontal planes shaded by normalized streamwise velocity ($\bar{U}/U_0$) taken in the cases of AR = 1 (top row), AR = 2 (middle row), and AR = 4 (bottom row) at the vertical location of 0.25h (left column), 0.5h (central column), and 0,75h (right column).

This traditional approach for horizontal plane selection which is based on a geometric parameter has limitations. In Figs. 4.12(a), (b) and (c), a significant difference in velocity contours can be observed since the selected planes for AR = 1 and 2 cut through the boundary layer (thickness, δ) at the height of 0.34δ and 0.7δ while, for AR = 4, the plane is outside of the boundary layer. The plane at the location z/h = 0.25 was selected with the purpose of analyzing the influence of the flow in the near-bed region, but Figs. 4.13(b) and (c) cannot capture the HSV. Similar drawbacks can be found in the comparison at other normalized selected elevations due to the inappropriate plane selection system. Overall, utilizing the traditional system to determine the elevation of the horizontal planes for analysis is not suitable and the selection of planes to compare the

characteristics at different aspect ratios needs to be reconsidered. In the following section, a new method of selecting the horizontal plane based on the pressure distribution will be introduced.

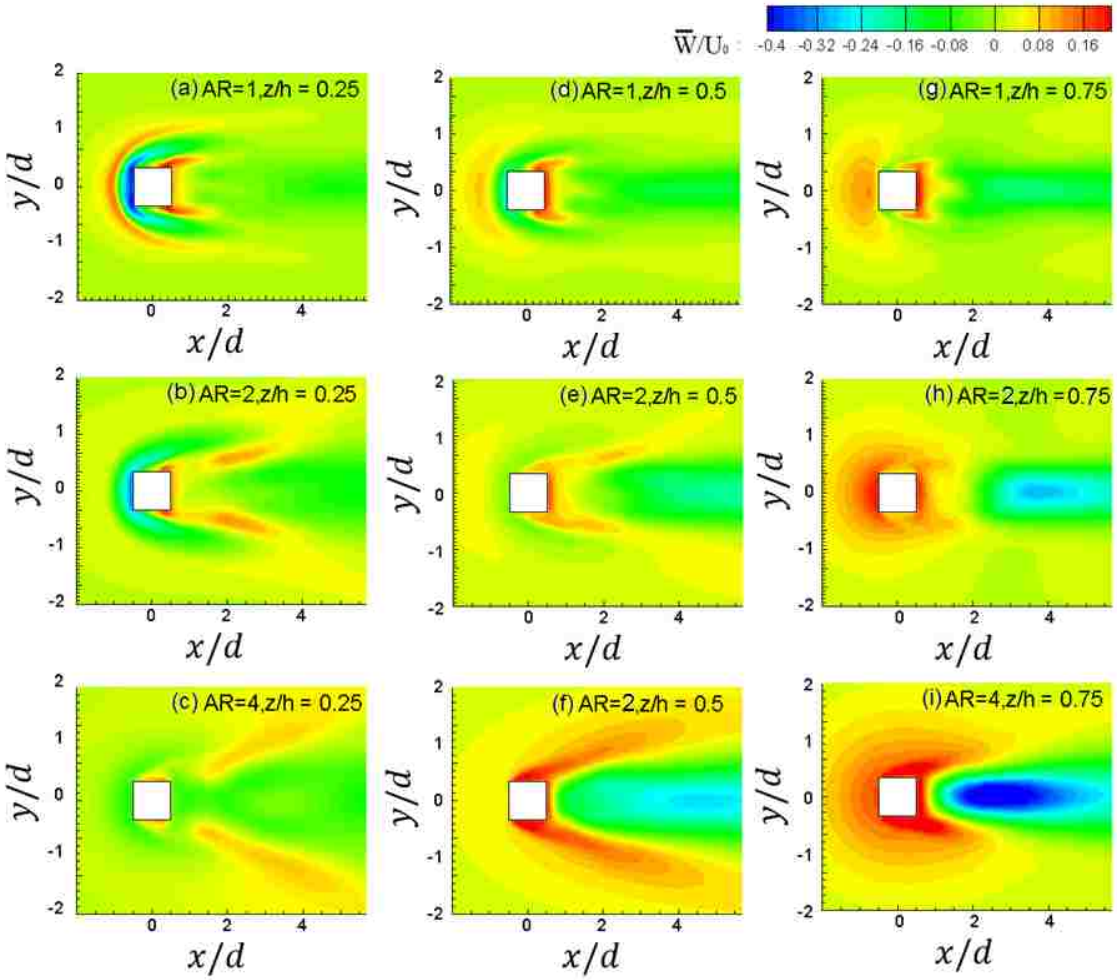

Figure 4.13 Horizontal planes shaded by normalized normal velocity ($\overline{W}/U_0$) taken in the cases of AR = 1 (top row), AR = 2 (middle row), and AR = 4 (bottom row) at the vertical location of 0.25h (left column), 0.5h (central column), and 0.75h (right column).

4.3.3 Time-averaged Pressure Distribution on the Central Plane of the Windward face

Figure 4.14(a) shows the pressure coefficient ($C_p = (P - P_0)/P_{stag}$) distribution on the windward face of the cylinder along the central plane (y/d = 0). From the figure, it is

clear that C_p varies with h. Starting at the bed, at each AR, the value of C_p decreases with increasing distance from the bed and attains a local minimum (marked as Point A in Fig. 4.14(a)). With further increase in z/h, C_p increases to a local maximum and then decreases towards the upper edge of the body. In the case of AR = 1, 2 and 4, the minimum C_p occurs at elevations corresponding to z/h = 0.21, 0.12 and 0.055, respectively. Although the elevations of the Point A normalized by the cylinder height (z/h) show a significant difference in each case, their location normalized by the cylinder width (z/d) are very close to each other, occurring at z/d = 0.21, 0.24 and 0.22, respectively. The decrease of C_p to a local minimum in the near-bed region can be ascribed to the effect of the horseshoe vortex (HSV). The location of Point A in terms of z/d remains similar since the HSV has been found to be of similar size at all AR values as indicated in the previous section.

Above Point A, C_p on the windward face of the cylinder increases towards the stagnation value. Seemingly, a distinct maximum can be found on the C_p plot for AR = 1, 2 and 4, at locations z/h = 0.7, 0.5 and 0.25, respectively. The locations are indicated as point B is the figure. Also, the C_p plot for AR = 4 shows a constant pressure zone from z/h = 0.2 to 0.8. The distinct stagnation point represented by maximum C_p in each case indicates that the incoming flow separates into a downward-oriented flow towards the bed and an upward-oriented flow towards the cylinder's free-end. Flow below point B is under the influence of the bed, and flow above this point is likely influenced by the free-end. The presence of the near-constant pressure zone found in the case of AR = 4 indicates that the incoming flow in this zone is not influenced by the bed nor the free-end.

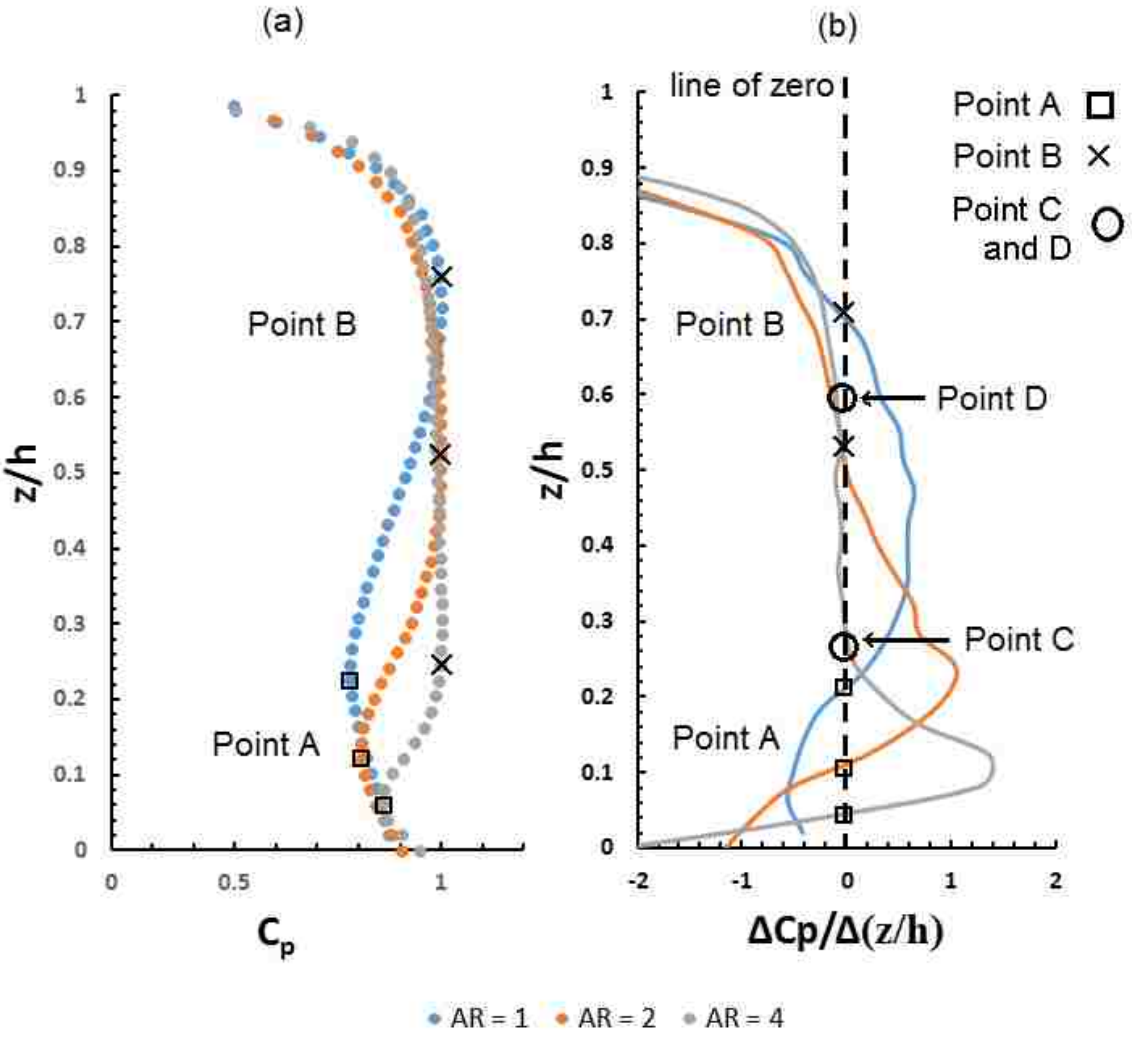

Figure 4.14 Pressure coefficient (C_p) distribution on (a) windward face of each cylinder; (b) derivative of the pressure coefficient with respect to vertical location ($\Delta C_p/\Delta(z/h)$)

The vertical location of the pressure maximum is determined by examining the change of the pressure coefficient with respect to the elevation, which is the derivative of pressure coefficient $\Delta C_p/\Delta(z/h)$, shown in Figure 4.14(b). By identifying the point where $\Delta C_p/\Delta(z/h) = 0$, this curve is capable of providing a more precise value for the location of Point B in the case of AR = 1 and 2. Also, this curve can be used to establish the two ends of the constant C_p region in the case of AR = 4 (marked as Point C and Point D, respectively). These two points are also critical because Point C denotes the lowest

elevation where the incoming flow impinges on the cylinder windward face, and Point D indicates where the flow starts accelerating due to the formation of the separating streamline above the cylinder's free-end.

By extracting the velocity field on the horizontal planes passing through Points A, and B (also Points C and D), the flow field at the selected planes for each AR is shown later to be more representative of the flow characteristics than that presented in section 4.3.2 since the horizontal planes have been selected based on the knowledge of the flow physics. Consequently, the comparison between different ARs on the planes crossing these critical points is likely to bring forth the influences on the flow field due to aspect ratio effects more directly than making such comparison based on traditional methods. As will be seen in the forthcoming sections, the flaws presented in section 4.3.2 are mostly eliminated by using the proposed method.

4.3.4 Time-averaged Velocity Field on Horizontal Planes (Pressure Distribution Method)

The normalized streamwise velocity ($\overline{U}/U_0$) field in the horizontal planes crossing Point A are shown in Figs. 4.15(a), (b) and (c). The common features that can be noted at all AR are the separating shear layers and the reverse flow in the wake region, identified by the red patches near the cylinder side-faces and the blue patch behind the cylinder, respectively.

Comparing the results at the three values of AR, it can be seen that $\overline{U}/U_0$ in the separating shear layer (presented as darker red patches) increases as the cylinder AR increases from 1 to 2. With further increase in AR to 4, the value of $\overline{U}/U_0$ in the shear layer region decreases, albeit slightly. It should be noted that the velocity in the approaching flow in the same horizontal plane varies slightly since the corresponding

elevation (0.21d, 0.24d and 0.22d for AR = 1, 2 and 4, respectively) also changes slightly. However, the differences noticed in the separating shear layer region cannot be entirely attributed to the change in the upstream velocity as the wake characteristics are also different and dependent on the aspect ratio.

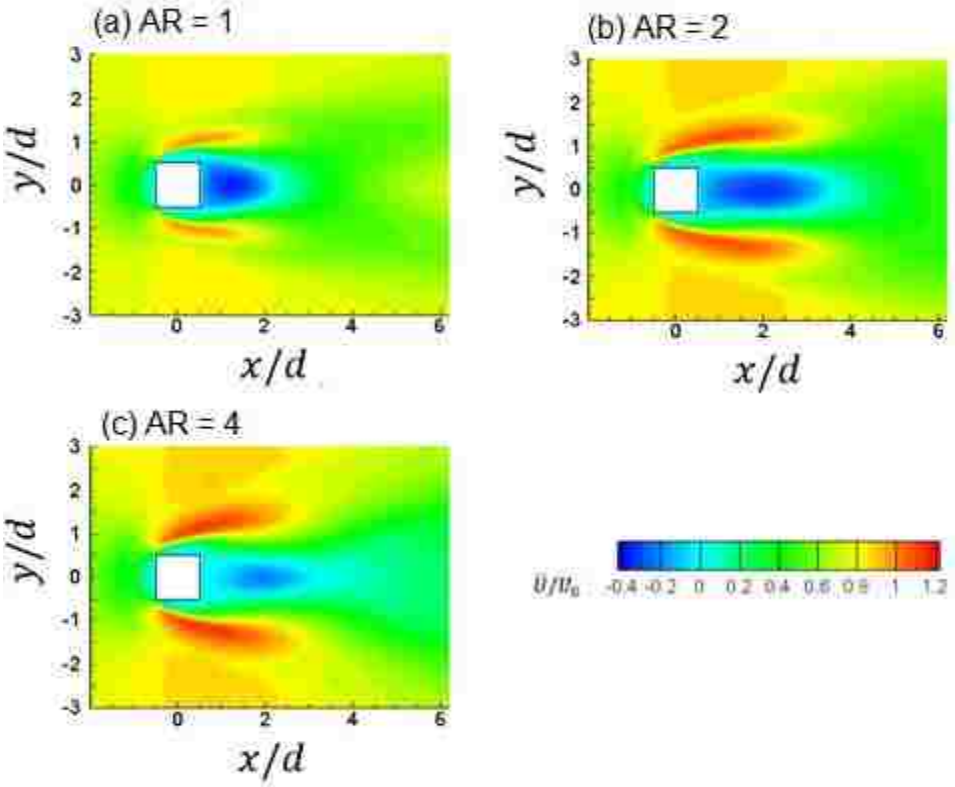

Figure 4.15 Horizontal planes through Point A, coloured by normalized streamwise velocity ($\bar{U}/U_0$): (a) AR = 1, (b) AR = 2, (c) AR = 4

The formation of the HSV hinders the incoming flow at the level of Point A from impinging onto the cylinder windward face, which is reflected as a local pressure coefficient minimum on the pressure distribution plot (Fig. 4.14). Since the fluid flow moves from a region of higher pressure to lower pressure, the incoming flow travels downwards from above to compensate the loss of fluid to the HSV formation, which matches the observation in the central plane shown in Fig. 4.2. Point B indicates the vertical location where the incoming flow below it moves entirely downwards. Point B is

located at z/d = 0.7 for AR = 1, while it is at z/d = 1 for both AR = 2 and 4. Judging by the distance from the bed to Point B, as the cylinder AR is increased from 1 to 2, a higher volume of fluid moves downwards, which consequently enhance the separating shear layer velocity. As the cylinder AR is further increased from 2 to 4, the volume of fluid that moves downwards remains unchanged. Therefore, the change in streamwise velocity noticed in the region of the separating shear layer at AR = 4 is perhaps more influenced by the near-bed wake characteristics.

A region of reverse flow (depicted by the blue patch downstream of the body in Fig. 4.15) can be observed in the wake region of each case. The flow entrainment into the wake is enhanced by a stronger separating shear layer. The presence of the downwash flow and the potential upwash from the near-bed region can also influence the size of the wake. These effects lead to a larger region of reverse flow found in AR = 2 than in AR = 1 cases in the plane through Point A. The reverse flow shown in the case of AR = 4 is weaker than that of AR = 2 due to the development of a stronger upwash flow shown in Fig. 4.2.

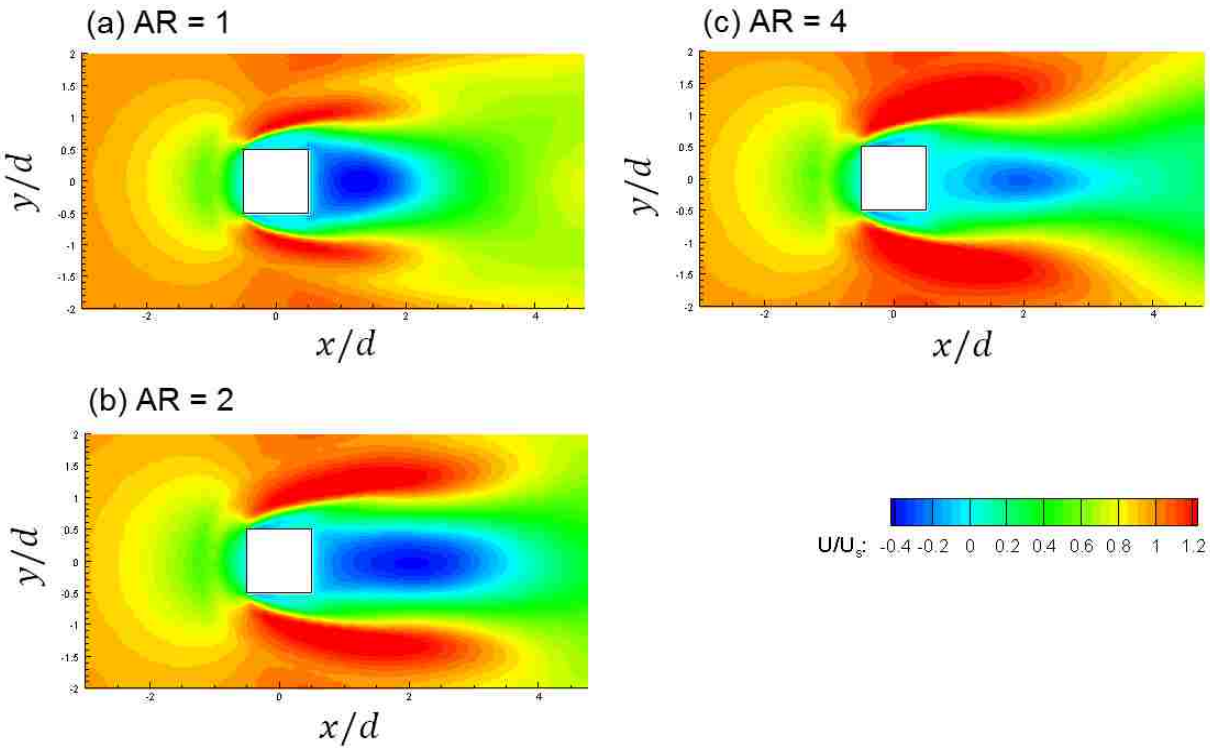

Figure 4.16 Horizontal planes through Point A, coloured by normalized streamwise velocity ($\bar{U}/U_s$): (a) AR = 1, (b) AR = 2, (c) AR = 4

Fig. 4.16 shows another representation of the time-averaged normalized streamwise velocity field through Point A. The corresponding approach flow velocity (U_s) at the level of Point A is used as the normalizing scale. All three contours have the similarities as discussed previously. Clearly, there are distinctive features in each of the flow fields that can be related to the aspect ratio effect.

Fig. 4.17 shows the contours of streamwise vorticity in the plane through Point A. It should be noted that the plane through Point A represents the region where the horseshoe vortex has a large impact on the windward face of each cylinder. The HSV is identified by negative (blue) and positive (red) patches around the body in each of the figures. At each AR, the horseshoe vortex is developed approximately at the same location in front of the body (x/d ~ -1). The extension of the HSV in the downstream flow

field is characterized by its spanwise width (from the outer edge of the blue region to the outer edge of the red region), the slope made by the legs of the HSV with the horizontal (slope value is indicated in the figure), merging point (MP, the downstream location where the HSV cannot be seen anymore, which means the HSV merges with the wake flow). The end of the near-wake region is indicated by S (where horizontal velocity is found to be zero along the wake axis). These values are indicated in Table 4.4.

Table 4.4 Characteristics of the HSV

AR	MP (x/d)	S (x/d)	HSV span	HSV slope
1	2.5	2.4	3d	0
2	3.5	3.8	4d	0.1
4	3	3	5d	0.18

As the cylinder AR is increased from 1 to 2, the location of both MP and S are farther downstream because the separating shear layer and the reverse flow become stronger. In the flow field of AR = 4, the separating streamline velocity is smaller than that at AR = 2 and the fluid entrained from the separating shear layer loses momentum to the development of the upwash structure (Fig. 4.2). Also, as discussed previously, the downwash flow is capable of further enhancing the fluid entrainment, which leads to a larger fluid circulation in the flow field for AR = 2. Therefore, the loss of momentum from upwash flow and the reduction in entrainment from the downwash flow results in S and MP being located closer to the body at AR = 4.

As the cylinder AR increases from 1 to 4, the results in Table 4.4 shows that the HSV span becomes wider, and the legs of the HSV develop a larger slope. It is evident that with increasing cylinder AR, there are significant changes to the HSV structure in the downstream region. The change in HSV can be related to factors including wake flow

structure and vortex shedding pattern. As the cylinder AR is increased from 1 to 2, the downwash flow which dominates the entire wake region increases in length (x-direction), indicated by a change in the location of S. Due to three-dimensionality of the flow field, the spanwise width (y-direction) of the wake is increased as well. As a result, Table 4.4 shows that the HSV span increases from 3d to 4d and the HSV slope increases from 0 to 0.1 as the cylinder AR is increased from 1 to 2. However, as the cylinder AR is increased to 4, the HSV span is further increased to 5d and the HSV slope is increased to 0.18, while the location of S comes closer to the cylinder leeward face which indicates that the length of the wake becomes smaller than AR = 2. This effect cannot be explained by the current time-averaged results.

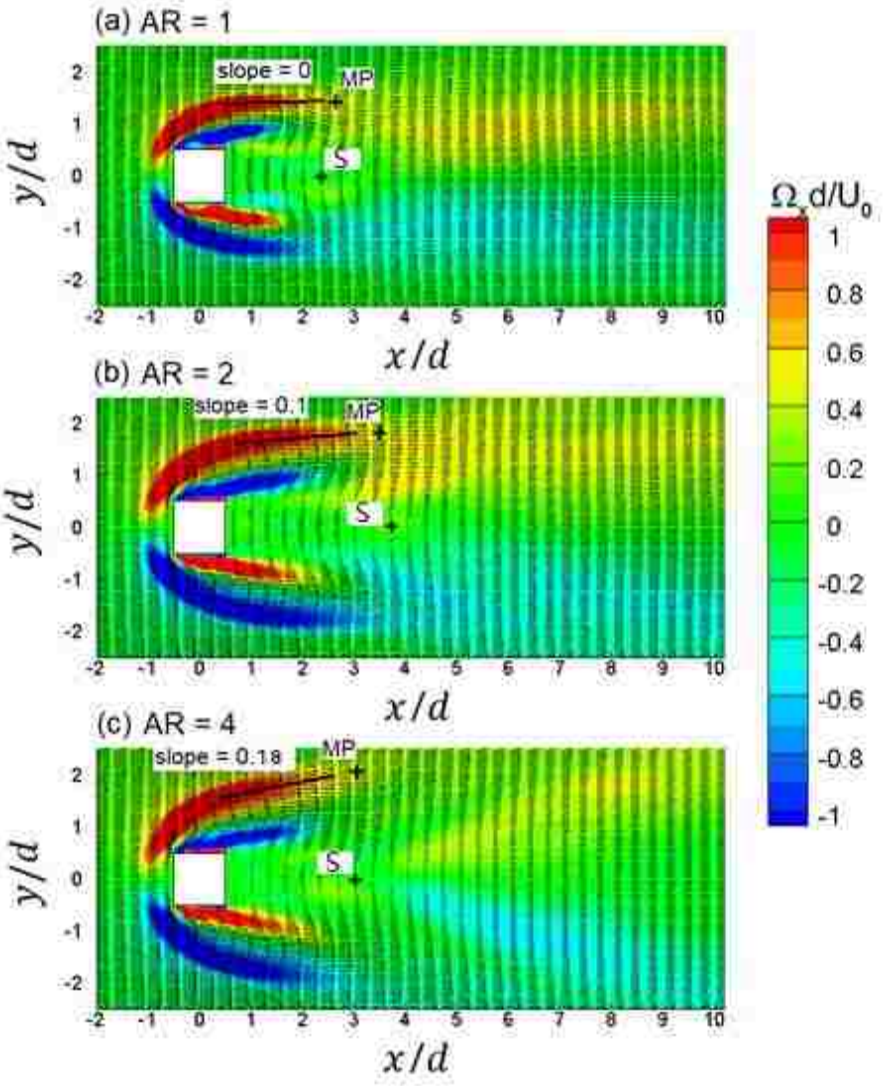

Figure 4.17 Horizontal planes through Point A coloured by normalized x-vorticity ($\Omega_x d/U_0$): (a) AR = 1, (b) AR = 2, (c) AR = 4

In the horizontal planes crossing Point B (Fig. 4.18), the streamwise flow field around the body presents a similar trend as seen in the planes crossing Point A. As the cylinder AR is increased from 1 to 2, the region occupied by the separating shear layer is enlarged with an increase in the streamwise velocity (contour changes from dark orange to red) as seen in Figs. 4.18(a) and (b). As the cylinder AR is further increased to 4, the separating shear layer remains similar in size and the increase in streamwise velocity is not significant. This can be explained by the plot of the change of pressure distribution in

Fig. 4.14 (b). In the figure, the curve for AR = 1 distinctly crosses the line of zero at Point B with a smaller slope than that noticed at AR = 2. This indicates that the incoming flow at the level of Point B for AR = 1 is strongly influenced by the flow field above and below. Unlike the curve for AR = 1, the curve of AR = 2 crosses the line of zero very gradually, and the curve of AR = 4 stays on the line of zero for a distance before crossing it. The influence from both ends of the cylinder for AR = 2 and 4 at the level of Point B is limited, which allows the incoming flow to freely accelerate towards the separation edge on each side. Therefore, in Fig. 4.18 at Point B, the separating shear layer on each side of the cylinder is significantly enhanced in terms of its size and flow velocity as the cylinder AR is increased from 1 to 2, but only subtle changes are observed with the further increase of the cylinder AR to 4.

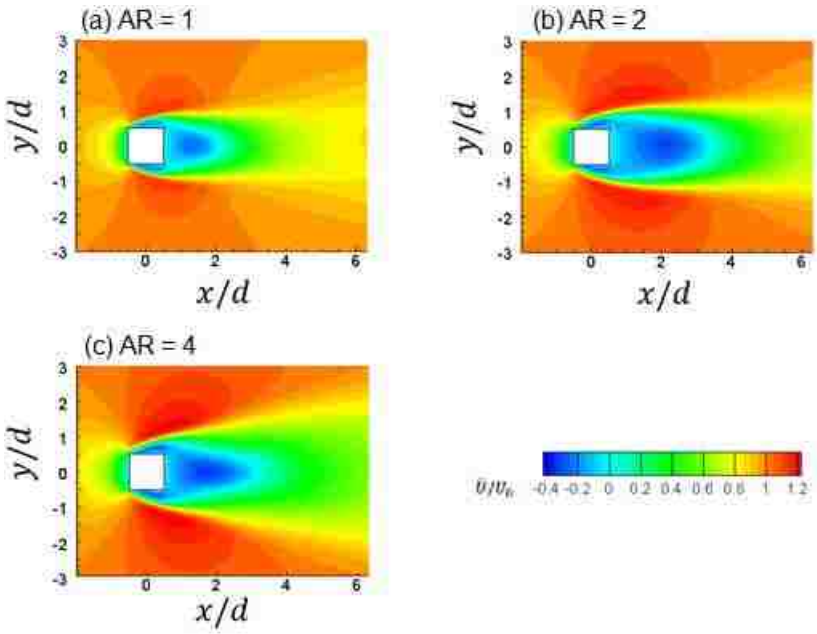

Figure 4.18 Horizontal planes through Point B, coloured by time-averaged normalized streamwise velocity ($\overline{U}/U_0$): (a) AR = 1, (b) AR = 2, (c) AR = 4

Also, it can be noticed that the flow field behind AR = 1 has a smaller and weaker reverse flow region at the level of Point B than that in the flow field behind AR = 2. This

is similar to the observation of the streamwise velocity in Fig. 4.15 at the level of Point A. However, unlike observations at the level of Point A, as the cylinder AR is further increased to AR = 4, the reverse flow on the plane through B does not become weaker. The flow velocity in the reverse flow region is roughly the same as at AR = 2, but the shape of the region is changed. The reverse flow region in the wake becomes narrow as the AR is increased from 2 to 4 due to the difference in fluid entrainment. To better understand the development of the near-wake, profiles at multiple downstream positions crossing the wake are presented in Fig. 4.19.

Fig. 4.19 plots the normalized streamwise velocity ($\overline{U}/U_0$) profiles at multiple locations (from x/d = 0.6 to 2.2 with an interval of 0.2). The profiles are symmetrical about the midplane y/d = 0. The streamwise velocity variation gradually changes from an inverted top-hat type profile across the inner wake region to a Gaussian type profile further downstream. The entrainment of high velocity fluid from the outer region into the inner region increases the streamwise velocity magnitude on the axis of symmetry. The inverted top-hat type profile starts close behind the cylinder's leeward face with a width of about 1d and ends at a location where the Gaussian type profile commences. In the present study, the wake flows at AR = 1 and 4 have a very short section of the top-hat type profile starting from the leeward face of the cylinder. The profile starts the transition to the Gaussian type profile from x/d = 0.8, and the transition is completed by x/d = 1.2. The wake flow for AR = 2 exhibits a much longer section of a top-hat type profile. The transition does not occur until after x/d = 1.2. At about x/d = 2.0, the transition is complete and the profile becomes a Gaussian type. This can be related to the downwash flow discussed in the vertical planes and the resulting three-dimensionality of the flow

field. In flow fields of AR = 1 and 4, the recirculation induced by the downwash is located very close to the cylinder's leeward face, which entrains more fluid into the wake and accelerates the transition process from a top-hat type to a Gaussian type profile in the downstream.

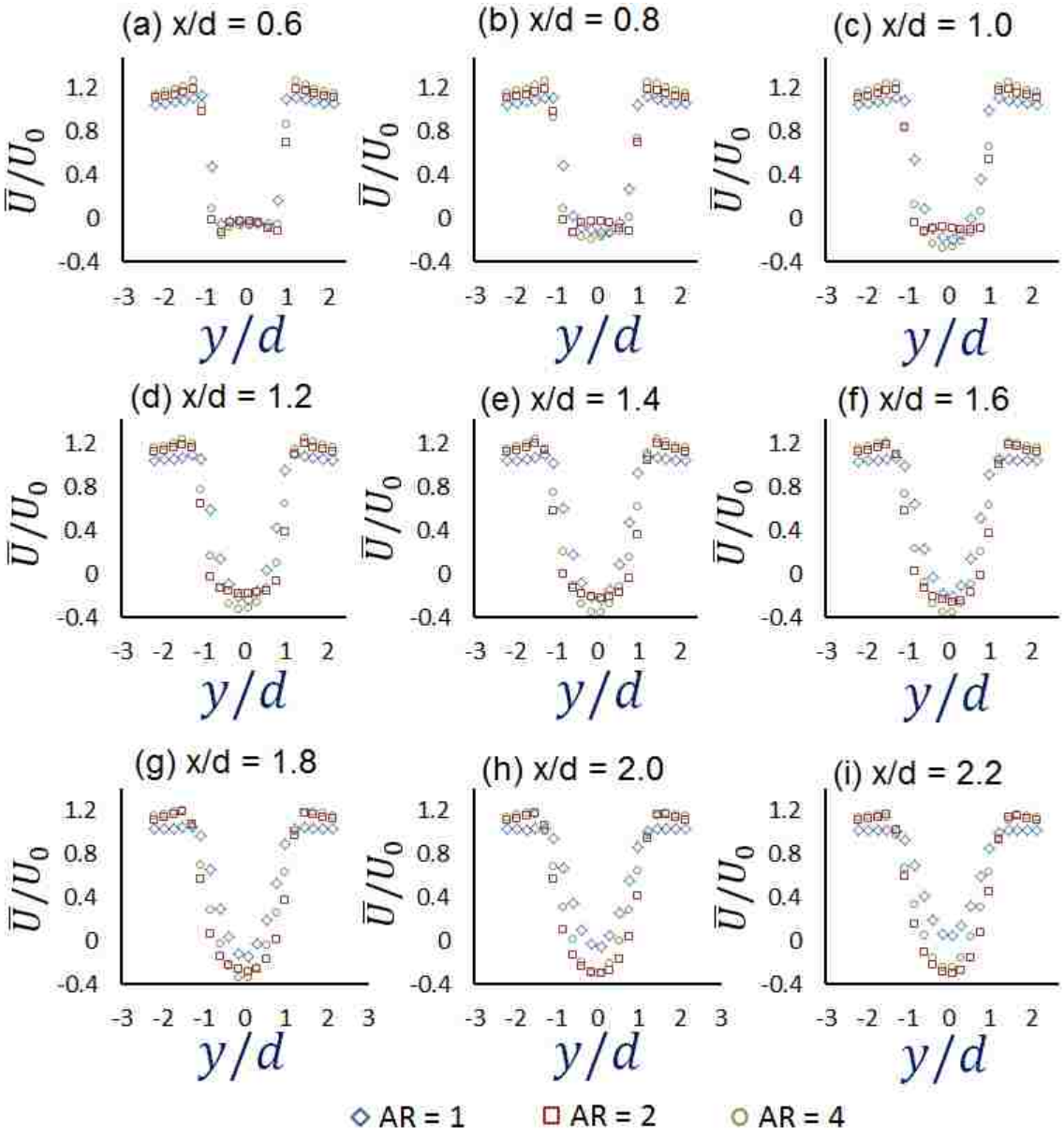

Figure 4.19 Time-averaged normalized streamwise velocity ($\bar{U}/U_0$) plots crossing the wake region of each cylinder from the downstream location of x/d = 0.6 to x/d = 2.2

The flow field around the cylinder with AR = 4 shows many differences compared to that observed around the cylinder with AR = 1 and 2, such as the development of the upwash flow in the wake shown in the central plane (Fig. 4.2(c)), inward spiralling recirculation shown in the central plane (Fig. 4.5) and existence of the constant pressure region (Fig. 4.14). These differences are due to the effect of aspect ratio which separates the flow near the free-end of the cylinder from that near the bed. In Section 4.3.3, the discussion on the plot of pressure distribution led to the introduction of two points, C and D. Point C denotes the start of the constant pressure zone while D denotes the end of the constant pressure zone. Note that Point C, in fact, is located at the same position as Point B, which is clearly the stagnation point for the lower values of AR. It is anticipated that the flow in the region of constant pressure is mostly unaffected by the features at the free-end and the bed region of the bluff body.

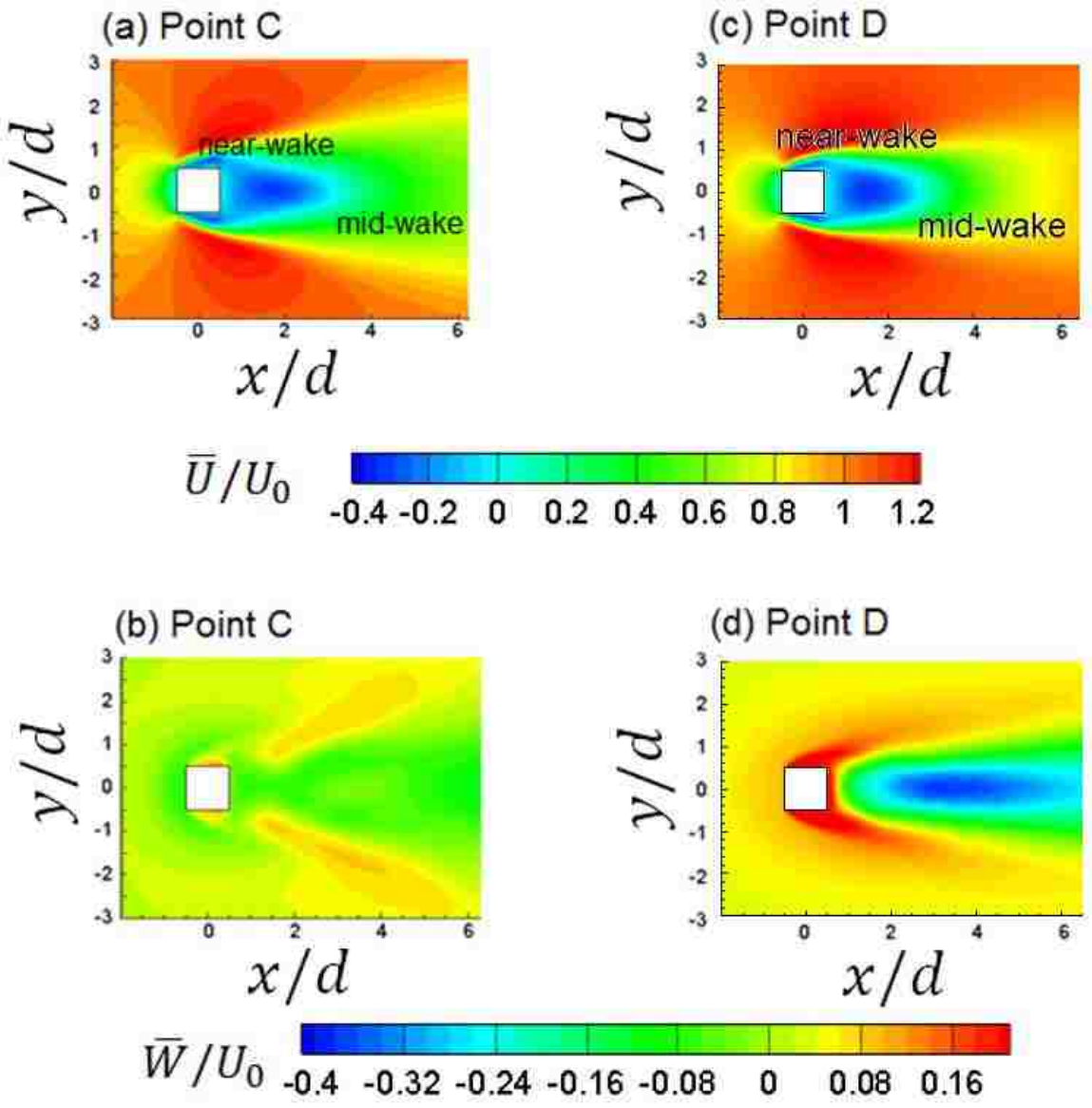

Figure 4.20 Horizontal planes through Point C (left column) and Point D (right column) for AR = 4 shaded by time-averaged normalized streamwise velocity ($\bar{U}/U_0$) (top row) and normalized normal velocity ($\bar{W}/U_0$)) (bottom row)

In Fig. 4.20, the normalized streamwise ($\bar{U}/U_0$) and normal ($\overline{W}/U_0$) velocity fields in horizontal planes crossing Point C and Point D are presented. The streamwise velocity contours in Figs. 4.20(a) and (c) show that the combined near-wake/mid-wake region at the location across Point D is smaller than that across Point C due to the influence of the cylinder's free-end. At the lower section of the wake shown in Fig.

4.20(b), the downward fluid momentum is transferred to the streamwise and spanwise directions. Therefore, the wake is larger in the streamwise velocity contour crossing Point C than that through Point D. Differences in the normal velocity contours can be observed in the horizontal plane crossing Points C and D shown in Fig. 4.20(b) and (d), respectively. The incoming flows near the windward face at two different levels move in opposite directions. Although the magnitude of the normal velocity is not high at both levels (approximately $0.08U_0$), it shows that Point C and Point D are at critical locations where the flow starts to accelerate towards the bed and the free-end, respectively. The wake region of the normal velocity contour at Point C and Point D are largely different. The horizontal plane crossing Point C in Fig. 4.20(c) is able to capture the top section of the upwash flow in the near-wake region. Slightly negative normal velocity is observed which is induced by the upwash flow. Two regions in the mid-wake show positive normal velocity which is indicative of the flow structure in the mid-wake/far-wake region that has not yet been discussed. This flow structure will be visualized in 3-D using the λ_2 criteria in Section 4.5. The horizontal plane through Point D is not able to capture this structure since Point D is relatively close the cylinder's free-end. The near-wake and mid-wake regions at the level of Point D is able to demonstrate the recirculation, where positive normal velocity is observed in the near-wake region and quickly drops to negative in the mid-wake region.

Compared to the conventional method of the horizontal plane selection shown in Figs. 4.12 and 4.13, the proposed method of plane selection can provide the following benefits:

1. When comparing the horizontal planes at Point A, the difference in the flow field due to the change of AR can be clearly illustrated, while maintaining the expected similarities based on the flow physics. Although the reverse flow region shows a different trend from AR = 2 to 4 than that from AR = 1 to 2, it has been noted that Point C and D should be introduced in the case where a constant pressure zone appears on the body's windward face.
2. The HSV in each case is captured by taking horizontal planes crossing Point A. The elevation of Point A indicates that the flow field at the corresponding level experiences the largest impact from the HSV. Thus, the influence of the HSV on the wake flow can be correctly examined and compared in each case.
3. At the level of Point B, the plots across the wake are capable of capturing the wake development. Because of the three-dimensional nature of the flow field, the wake development can be directly related to the downwash flow and its recirculation. Comparing the plots in each case, the effect of AR on the wake development can be realized.

A critical value of AR has been noted. By examine the time-averaged flow field, many flow features in the case of AR = 4 are different than in the case of AR = 1 and 2. A categorization method has been introduced in this section by the existence of a constant pressure zone. In the case when a constant pressure zone is found on the windward face of the body, Point C and Point D should be introduced to better characterize the flow field. Even though the current study lacks data at larger values of AR where a constant pressure zone exists, a comparison of the flow field in the horizontal planes crossing Point C and Point D may be worthwhile.

4.3.5 Time-averaged Vorticity and Velocity Fluctuation on Central Planes

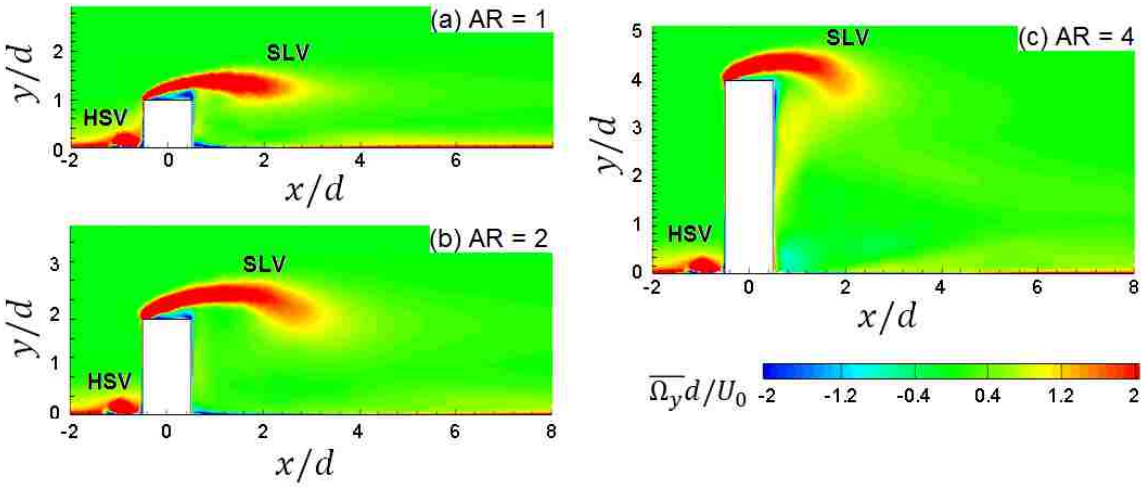

Figure 4.21 Time-averaged normalized spanwise vorticity ($\overline{\Omega_y}d/U_0$) contours in the central plane: (a) AR = 1, (b) AR = 2, (c) AR = 4

Fig. 4.21 presents the time-averaged normalized spanwise vorticity ($\overline{\Omega_y}d/U_0$) in the central plane of the three cylinders. Two significant fluid structures are illustrated in each plot: the central cross-section of the HSV represented by a red patch in front of each cylinder near the bed and a shear layer above the cylinder free-end. As discussed previously, the size of the HSV in the central plane is similar for all three cases. The shear layer above the cylinder free-end shows similar traits as previously observed from the streamtraces. As the cylinder AR is increased from 1 to 2, the shear layer extends further downstream due to the increase in momentum gained from the flow separation. As the cylinder AR is further increased to 4, the tip of the shear layer lies closer to the cylinder. Instead of extending further, similar to the observation of the streamtraces, the shear layer moves downwards almost immediately after it passes the cylinder.

Recalling Fig. 4.5, which illustrates the recirculation formed in the near wake of each cylinder, both recirculation vortices of AR = 1 and 2 are outward-spiraling. However, the flow at AR = 4 has an inward-spiraling vortex in the wake region. The

outward-spiraling vortex shows that the recirculation is acting as a source which takes entrained fluid from the sides to push the flow from the top further downstream. As a result, the shear layer of AR = 1 and 2 at the cylinder free-end does not curl down right after it passes the cylinder, but extends further downstream. In the flow field at AR = 4, the recirculation is similar to a sink which takes the flow from the cylinder free-end into the near-wake region. Therefore, as observed in Fig. 4.21(c), the shear layer curls downwards immediately after it passes the cylinder.

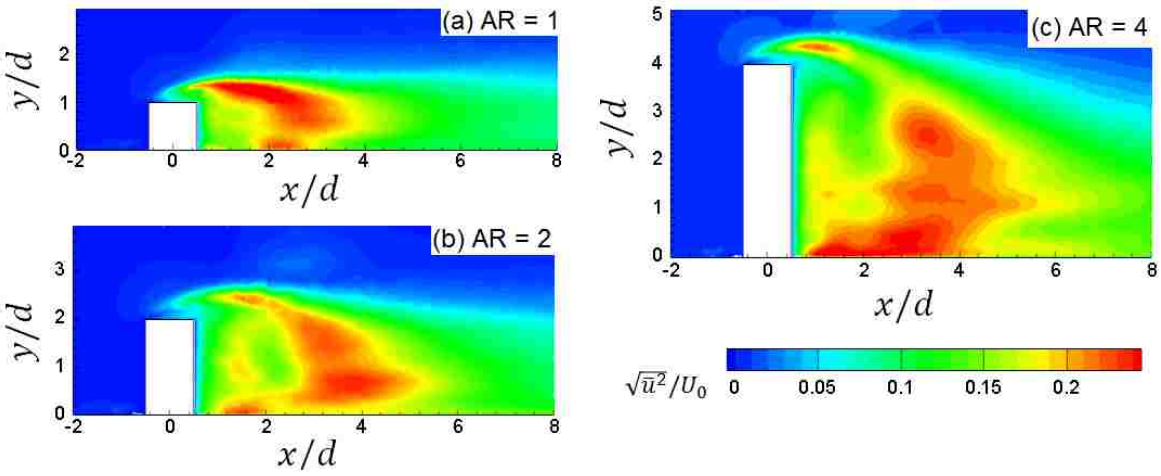

Figure 4.22 Normalized streamwise turbulence intensity ($\sqrt{\overline{u^2}}/U_0$) contours in the central plane: (a) AR = 1, (b) AR = 2, (c) AR = 4

Figs. 4.22 and 4.23 shows the contours of streamwise and normal turbulence intensity normalized by the free-stream velocity ($\sqrt{\overline{u^2}}/U_0$ and $\sqrt{\overline{w^2}}/U_0$), respectively. In the flow field of AR = 1 shown in Fig. 4.22(a), a higher value of streamwise turbulence intensity can be found along the separating streamline after it passes the cylinder. The outward-spiraling recirculation observed in the near-wake of AR = 1 sends the flow outwards and mixes with the separating shear layer above the cylinder, which results in high values of streamwise fluctuations as shown in Fig. 4.22(a). Between x/d = 2 and 3

on the bed, a small region with a high value of $\sqrt{\overline{u^2}}/U_0$ is noticed. This is the location where the downwash flow impinges on the bed as seen in the velocity contours in Fig. 4.2(a). High value of streamwise turbulence intensity is expected near the saddle point since the downwash flow tends to move downstream but the recirculation pulls the near-wake flow towards the body. High value of normal turbulence intensity can be observed in the mid-wake region since this is where the interaction between the shear layer and the flow in the near-bed region occurs (Fig. 4.23(a)).

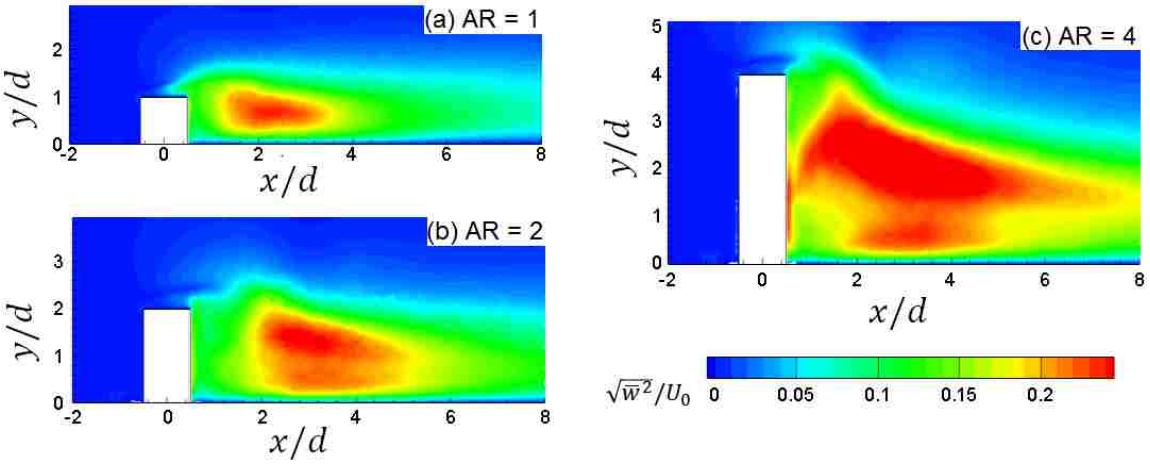

Figure 4.23 Normalized normal turbulence intensity ($\sqrt{\overline{w^2}}/U_0$) contours in the central plane: (a) AR = 1, (b) AR = 2, (c) AR = 4.

In the flow field of AR = 2 (Fig. 4.22(b)), the high value of streamwise turbulence intensity can be found in the separating streamline region as the flow passes the cylinder free-end. Unlike the flow field at AR = 1, largest fluctuations are found closer to the bed in the region x/d = 3 to 5. This indicates that the shear layer from the free-end of the cylinder is able to move downwards due to the increasing distance between the free-end and the bed. The highest fluctuations are found close to the saddle point presented in Fig. 4.2(b). A smaller sized red patch can be observed on the bed at x/d = 2. This suggests that

the flow at the near-bed level becomes stronger, which means an upwash flow starts developing, although it is not distinctly observed in the time-averaged velocity field. Fig. 4.23(b) shows that the normal velocity fluctuations for AR = 2 are similar to those seen for AR = 1, where the high value of normal turbulence intensity is found in the mid-wake region due to the interaction between the shear layer and the flow in the near-bed region.

In the flow field of AR = 4 (Fig. 4.22(c)), similar to the flow field of AR = 2, a region with high streamwise velocity fluctuation can be found along the separating streamline after it passes the cylinder free-end. As the shear layer curls downwards, streamwise velocity fluctuation starts to increase at approximately 3d above the bed in the mid-wake region. At the level about 1.2d, the region with high streamwise velocity fluctuations becomes the largest. The fluctuations in this region are induced by the interaction between the shear layer and the flow in the near-bed region as this region is located in the vicinity of the saddle point as shown in Fig. 4.2(c). A large region with high streamwise velocity fluctuations is located in the near-bed region where the upwash structure is identified by the streamtraces. The contours of streamwise fluctuations in Fig. 4.22(c) show that the upwash structure is highly turbulent in the streamwise direction. In the normal turbulence intensity contours shown in Fig. 4.23(c), the region near the saddle point is highly turbulent. Different from AR = 1 and 2, where a high level of normal turbulence intensity is observed in the mid-wake region, a high level of normal turbulence intensity is also observed in the near-wake of AR = 4 immediately behind the body. This is the result of the downwash flow entering the near-wake and impinging on the leeward face of the cylinder.

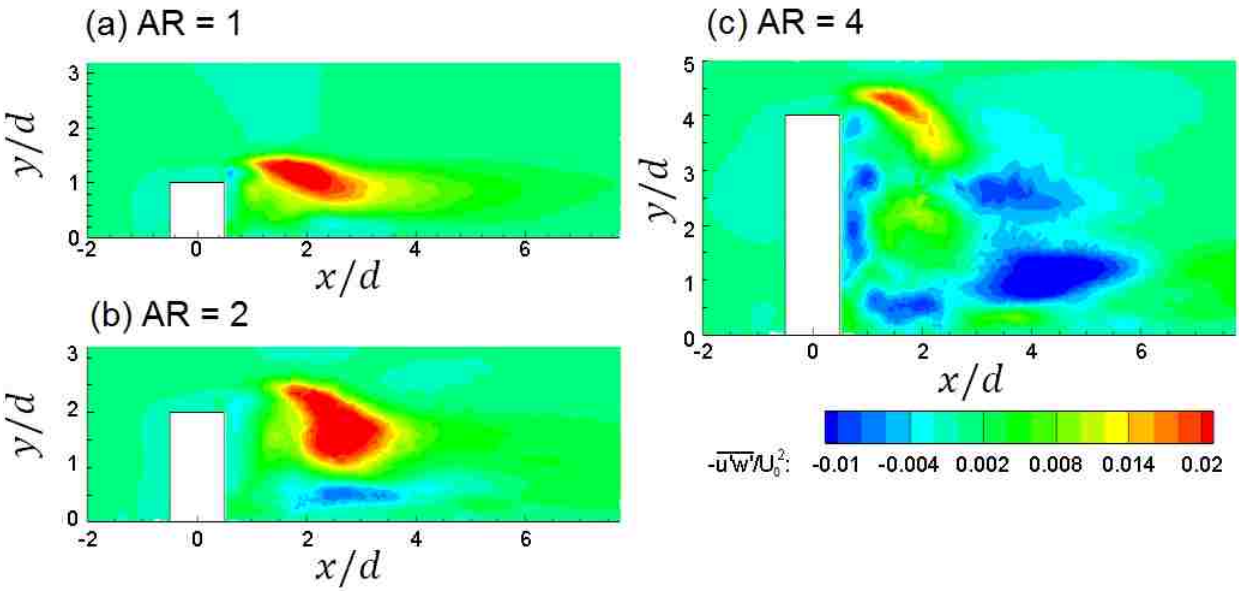

Figure 4.24 Normalized Reynolds shear stress $-\overline{u'w'}/{U_0}^2$ contours in the central plane: (a) AR = 1, (b) AR = 2, (c) AR = 4.

Fig. 4.24 shows the Reynolds shear stress ($-\overline{u'w'}/U_0^2$) contours in the central plane of each flow field. In each contour, the separating streamline creates positive shear stress approximately at the level of the cylinder free-end in the wake region. In the flow field for AR = 1, the contour is observed to extend downstream. In the flow field of AR = 2, the region with strong shear stress becomes larger, but expands in the near-wake/mid-wake region. A region with negative Reynolds shear stress can be observed in the near-bed region, which is evidence of the upwash flow. In the flow field for AR = 4, the region with positive shear stress appears to be significantly smaller than AR = 1 and 2. This may be explained as the downwash flow freely entering the near-wake region and forming the recirculation, as opposed to AR = 1 and 2, where part of the downwash flow travels downstream. Regions with negative Reynolds shear stress are found near the leeward face of the cylinder and the bed, indicating that flows in these regions are highly turbulent due to the mixing of the separating streamline from the free-end and the shear layers both sides of the cylinder. As the cylinder AR is increased, the increasing negative

Reynolds shear stress observed in the near-bed region also indicates that the mass transport is enhanced.

4.4 Instantaneous Spanwise Vorticity on Central Planes

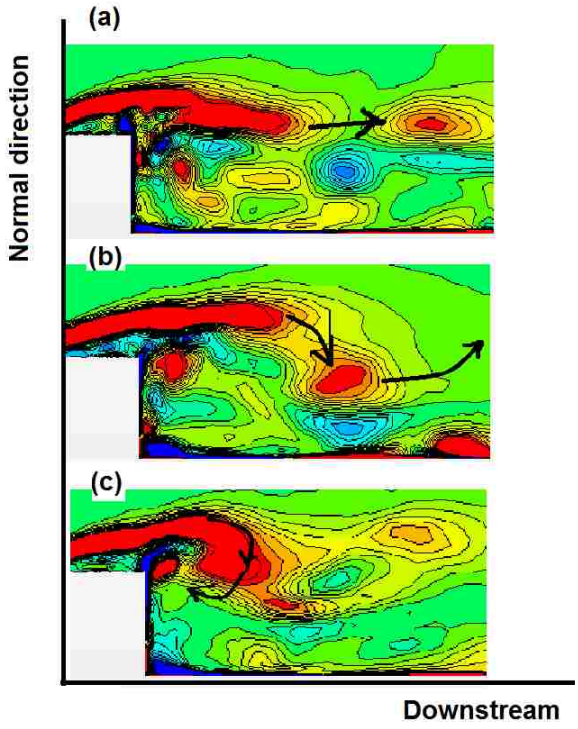

Figure 4.25 Instantaneous flow field for AR = 1 coloured by spanwise vorticity ($\overline{\Omega_y} \times d/U_0$): (a) shed vortex from the shear layer travels downstream; (b) shed vortex from the shear layer moves downward then travels downstream; (c) shed vortex from the shear layer curls and enters the near-wake

Figs. 4.25-4.27 show the spanwise vorticity on the central plane in the near-wake of each cylinder. In each of these figures, the high-vorticity shear layer can be clearly tracked. The analysis presented below is composed of information that is observed from many fields-of-view over a large time period. In each figure, three instances which represent different scenarios of the vortex shedding process are illustrated.

In the flow field of AR = 1, the shed vortex moves horizontally downstream with very little interference from the bed as shown in Fig. 4.25(a). Occasionally, the shed

vortex travels downwards at first, then the flow in the near-bed region pushes the shed vortex upwards as observed in Fig. 4.25(b). These two scenarios occur most frequently in the flow field. Fig. 4.25(c) shows a rare occasion where the shear layer curls up and forms the recirculation instead of traveling downstream. This occurs much less frequently than (a) and (b), so it is neither represented in the time-averaged y-vorticity contours nor in the streamtraces shown earlier (the curling motion of the shear layer is represented by an inward-spiraling recirculation).

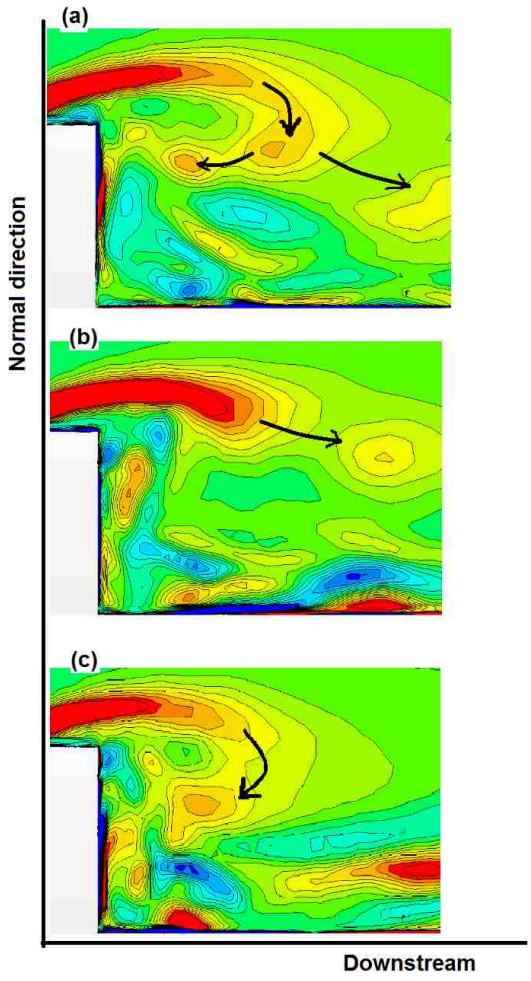

Figure 4.26 Instantaneous flow field for AR = 2 coloured by spanwise vorticity ($\overline{\Omega_y} \times d/U_0$): (a) shed vortex from the shear layer splits into two vortices, one travels downstream and one enters the near-wake; (b) shed vortex from the shear layer moves

downward then travels downstream; (c) shed vortex from the shear layer curls and enters the near-wake

Fig. 4.26 shows three instances of the flow field for AR = 2 where vortex shedding patterns are different in each case. As shown in the time-averaged spanwise vorticity contours in Fig. 4.21(b), in each of the cases shown in Fig. 4.26, the well-formed shear layer travels downstream for a short distance then moves towards the bed. The most frequent behavior is presented in Fig. 4.26(a). The vortex shed from the shear layer breaks into two (or two groups) of vortices, one curls into the near-wake and one travels downstream. The splitting of the vortex causes the high streamwise velocity fluctuations in the mid-wake region observed in Fig. 4.22(b). By visually observing different fields-of-view it was noticed that either one of the split vortical structures may not occur at some instances. Fig. 4.26(b) shows that the shed vortex travels directly downstream, which resembles Fig. 4.25(a) in the flow field of AR = 1. Fig. 4.26(c) shows the shed vortex from the shear layer entering the near-wake of the flow field, which resembles Fig. 4.25(c) in the flow field of AR = 1.

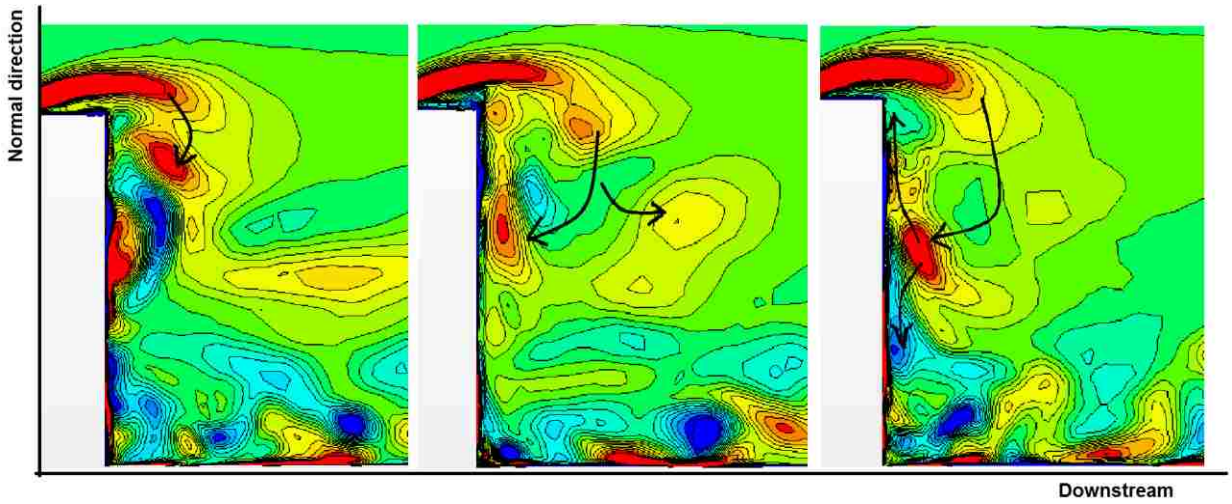

Figure 4.27 Instantaneous flow field for AR = 4 coloured by spanwise vorticity ($\overline{\Omega_y} \times d/U_0$): (a) shed vortex from the shear layer curls and enters the near wake; (b) shed vortex from the shear layer splits into two vortices,; (c) shed vortex from the shear layer splits into two vortices on the leeward face of the cylinder

Fig. 4.27 shows three instances of the flow field for AR = 4 where the vortex shedding patterns are slightly different. In all scenarios presented in Fig. 4.27, the shear layer curls downwards right after it passes the cylinder, which resembles a time-averaged y-vorticity contour of AR = 4 in Fig. 4.21. Fig. 4.27(a) shows the entire shed vortex enters the near-wake and forms the recirculation and Fig. 4.27(b) shows that the shed vortex is split into two smaller vortical structures, where one travels towards the body while the other moves downstream. These two patterns of vortex shedding are similar to that shown in Fig. 4.26(a) and (c) for AR = 2, but the pattern of Fig. 4.27(b) is less frequently observed. Fig. 4.27(c) shows one pattern that is not found in the flow fields of AR = 1 and 2, which represents the direction of flow towards the leeward face of the cylinder. As the shed vortex curls into the near-wake and approaches the leeward face of the cylinder, it splits into two vortical structures, one of which moves upwards and the other downwards as shown in the figure. By observing different images of the flow field, the location of the reattachment is found to be oscillating and close to half-height of the

cylinder (z/d = 2). The vortical structure moving upward forms the recirculation, and the one moving downwards mixes with the upwash flow in the near-bed region. This vortex shedding pattern occurs frequently enough that it makes a significant impact on the contours of $\sqrt{\overline{w^2}}/U_0$ and $-\overline{u'w'}/{U_0}^2$ in Figs. 4.23 and 4.24.

As the cylinder AR is increased from 1 to 2, the vortices from the shear layer are more likely to enter into the near-wake, and less likely to travel downstream directly. This is consistent with the findings from the streamtraces of the recirculation in the central plane. The outward-spiraling recirculation is weakened as the cylinder AR is increased from 1 to 2, which represents an increasing time for the fluid inside the vortex to reach the periphery. As the cylinder AR is further increased to 4, the outward-spiraling recirculation is completed replaced by the inward-spiraling vortex. This is reflected in most of the instances when the shedding occurs and enters the wake. Rarely, a small portion of the shed vortex moves downstream directly in the flow field of AR = 4.This commonly occurs for AR = 1 and 2.

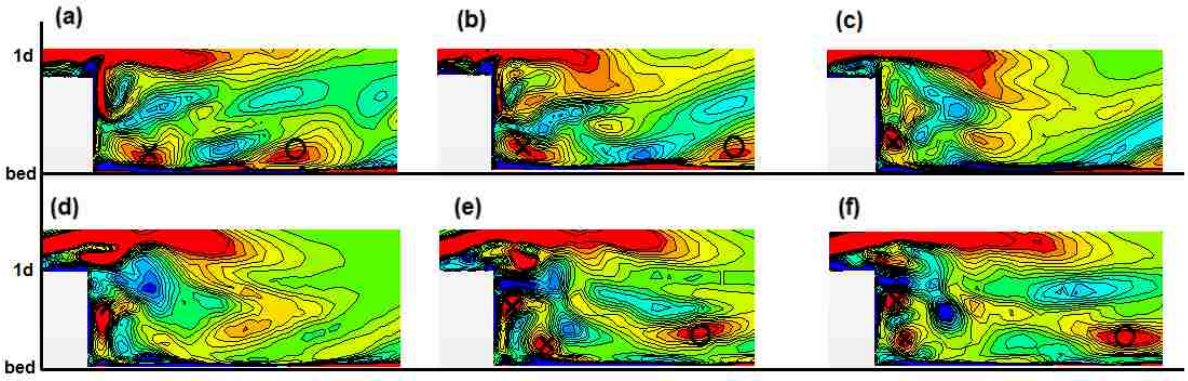

Figure 4.28 Consecutive instantaneous flow fields for AR = 1 in the central plane with 0.001s between each field-of-view coloured by spanwise vorticity ($\overline{\Omega_y} \times d/U_0$)

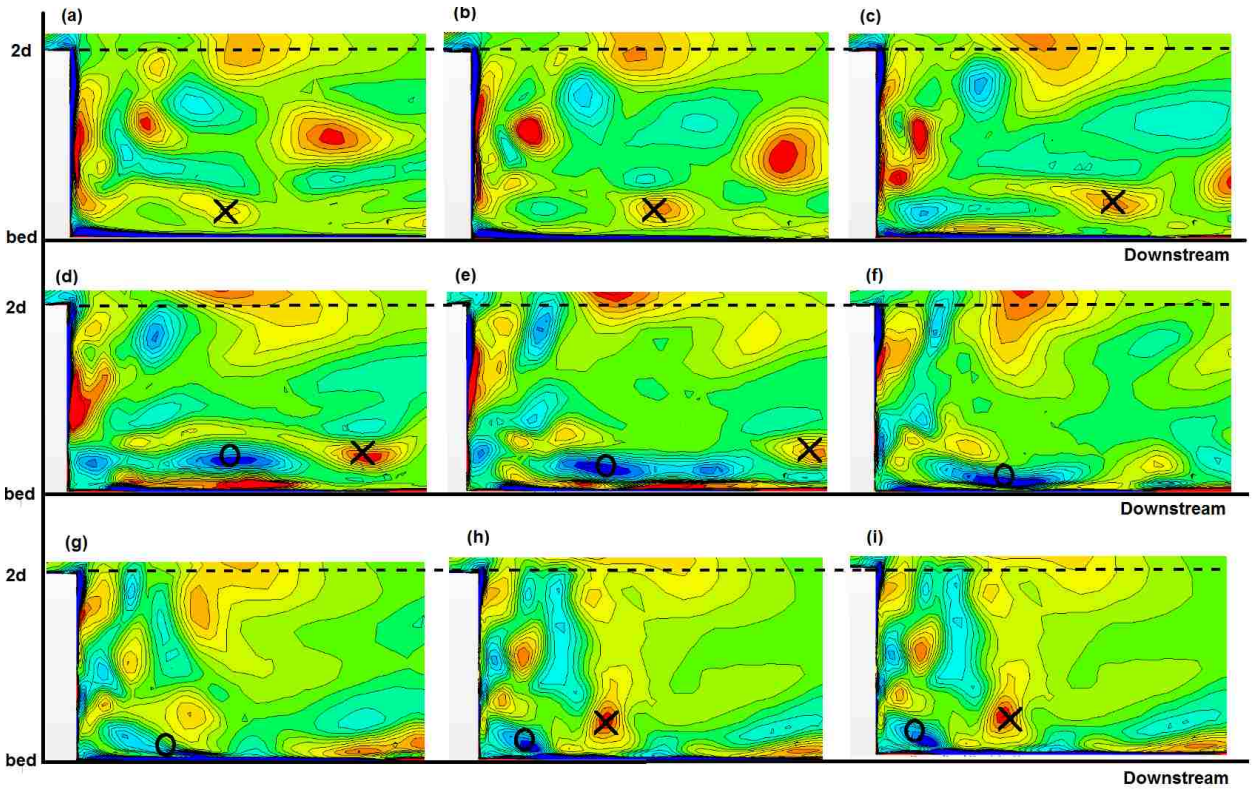

Figure 4.29 Consecutive instantaneous flow fields for AR = 2 in the central plane with 0.001s between each field-of-view coloured by spanwise vorticity ($\overline{\Omega_y} \times d/U_0$)

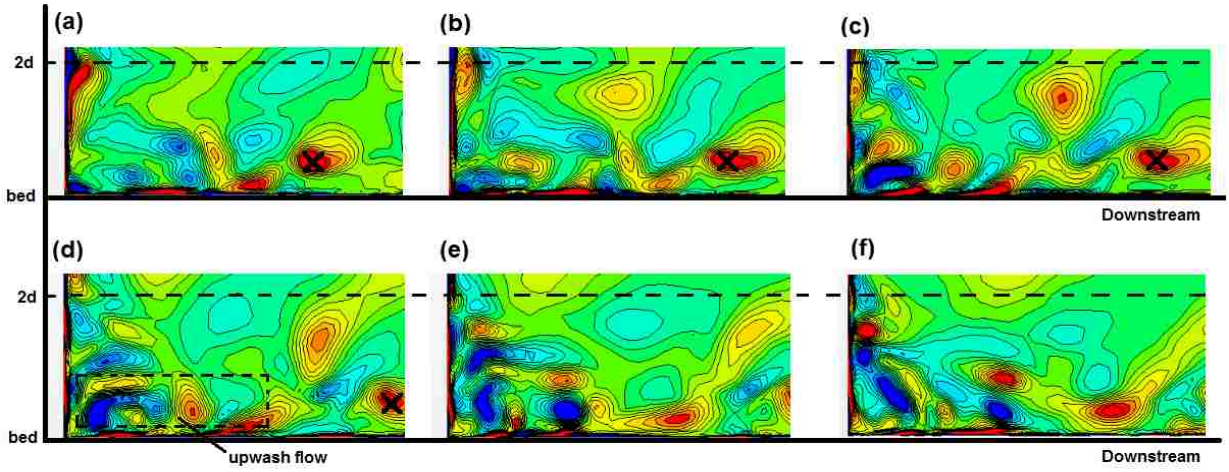

Figure 4.30 Consecutive instantaneous flow fields for AR = 4 in the central plane with 0.001s between each field-of-view coloured by spanwise vorticity ($\overline{\Omega_y} \times d/U_0$)

Figs. 4.28 – 4.30 contain instantaneous spanwise vorticity contours which focus on the near-wake and near-bed regions in the flow fields of AR = 1, 2 and 4, respectively,

with the purpose of examining the evolvement of the upwash flow. After scanning through a large number of consecutive samples of each flow field, it is apparent that the flow in the near-bed region is significantly more chaotic than the shed vortex from the separating shear illustrated in Figs. 4.28 – 4.30. Figs. 4.28 – 4.30 shows a selected few consecutive flow fields with 0.001s interval (~1/8T, T is the vortex shedding period) with the aim of demonstrating the dominant movement of the near-bed vortices.

In Fig. 4.28 for AR = 1, a vortex developed in the near-bed region with positive spanwise vorticity (marked by "X") is shown in the flow field from (a) to (d). In the selected instances, this vortex, which develops in the near-bed region (as shown in (a)) gradually enters the recirculation region (as shown in (b-f)) and moves towards the upper edge of the bluff body. In Fig. 4.28(e) and (f), another vortex with positive vorticity developed in the near-bed region can be observed. It shows a similar path as the vortex observed in (a). A vortex marked by "O" which travels downstream can also be observed in the fields-of-view presented. This vortex is developed roughly at the same time as the vortex marked by "X", as shown in both (a) and (e). Fig. 4.29 shows the near-bed vortices of the flow field for AR = 2. Marked by "X" in Fig. 4.29(a) to (e), the vortex with positive spanwise vorticity travels downstream. Another vortex with negative vorticity marked by "O" in Fig. 4.29(d) to (i), shows a different path, moving closer to the leeward face of the cylinder and staying at the near-bed level. The vortex with negative vorticity is trapped in this region of the flow field. The existence of this vortex can be seen as a sign of the development of the upwash flow. Fig. 4.30 shows the near-bed region for AR = 4. The upwash shown in the dotted box is present in most of fields-of-view. However, the flow in this region is highly turbulent as demonstrated by the

unsteady vortices. This matches with Figure 4.22 which shows that high value of streamwise fluctuations is located in the near-bed region for AR = 4. Similar to the flow field for AR = 2, a vortex with positive vorticity marked by "X" can be found traveling downstream.

As the cylinder AR is increased from 1 to 2, the vortices developed in the near-bed region tend to leave the near-wake region. The flow in the near-wake region is more frequently supplied by the shear layer from the cylinder free-end, as discussed previously in Fig. 4.26. Also, the vortices with negative vorticity that are trapped in the near-wake region create velocity fluctuations and turbulence in the near-bed region of AR = 2. As the cylinder AR is further increased to 4, the highly turbulent zone, which is attributed to the upwash flow, constantly appears in the near-bed and near-wake regions of the flow field. The flow in the near-bed region becomes highly unsteady and chaotic as the cylinder AR is increased. The near-bed region can be crucial since it may be related with pedestrian comfort in building design or heat transfer rate in electronic component design. Further investigation with the aim of distinguishing coherent and incoherent structures in the near-bed region can be conducted to gain a better knowledge of the flow field.

4.5 3-D Visualization by the λ_2 Criterion

In the current study, the λ_2 criterion is utilized for flow visualization [31]. This method defines a vortex core as a connected region with two negative eigenvalues of the pressure Hessian ($S_T{}^2 + \Omega_T{}^2$), where S_T is the strain tensor and Ω_T is the rotational tensor. The tensors S_T and Ω_T are defined as:

$$S_{T\ i,j} = \frac{1}{2}\left(\frac{\partial \bar{U}_i}{\partial X_j} + \frac{\partial \bar{U}_j}{\partial X_i}\right)$$

$$\Omega_{T_{i,j}} = \frac{1}{2}\left(\frac{\partial \overline{U}_i}{\partial X_j} - \frac{\partial \overline{U}_j}{\partial X_i}\right)$$

where $\overline{U}_i$ is the time-averaged velocity in the X_i direction. The second eigenvalue, commonly referred to as λ_2, is utilized to create an iso-surface for the time-averaged flow field around each cylinder with a value of -0.005, shown in Figs. 4.31 – 4.33. In each figure, the oblique view, top view, side view and back view of the flow field are presented in top-left, top-right, bottom-left and bottom right, respectively. The 3-D iso-surface plot is able to support the findings noticed in the previous sections. The vortical structures of the HSV and the shear layer in the near-wake/mid-wake can be clearly observed in each figure from different points of view. The iso-surface of the flow field for AR = 4 provided by Bourgeois et al. [9] matches well with the results shown in Fig. 4.31, which further validates the simulation results in the current study.

In the mid-wake/far-wake region of each flow field, two vortex tubes extending downstream are formed due to the Biot-Savart induction by the downwash flow and the shear layers from each side [9]. Researchers concluded that the streamwise vortex tubes present a dipole type (one pair of counter-rotating streamwise vortex tubes) when the cylinder AR is small, and a quadrupole type (two pairs of counter-rotating streamwise vortex tubes) when the cylinder AR is above a critical value [3], [4]. In the present study, the streamwise vortex tubes shown are all dipole type. A pair of smaller vortical structures can be found in the wake of AR = 4 underneath the larger tubes. However, the streamwise vorticity of this pair is in the same direction as the larger tubes above. Bourgeois et al. [9] stated that the smaller vortical structures on each side are of the same structure as the large vortex tubes, which is clearly not a quadrupole type. Thereby, the

time-averaged vortical structure in the mid-wake/far-wake region for each cylinder AR is approximately the same as shown in Figs. 4.31 – 4.33.

Some differences in the streamwise vortex tubes can be observed in Figs. 4.31 – 4.33 as the cylinder AR varies. In Figs. 4.32 and 4.33 for AR = 1 and 2, the vortex tubes are attached to the bed, as opposed to Fig. 4.31 for AR = 4, the tubes are observed to be levitated because the core of each tube for AR = 4 is located at a higher elevation. Hence, the near-bed region of the far field is strongly influenced by the streamwise vortex tubes. Recall the discussion in Section 4.3.4 on HSV observed in the horizontal plane at Point A, the HSV was observed to have a larger span and opens out wider (with a large slope) as the cylinder AR increases. This effect is likely to be induced by the elevation of the cores of the vortex tubes. As the core of the vortices are located in the near-bed region for AR = 1 and 2, the HSV extension and the corresponding vortex tube merge and bring the HSV extension toward the centerline (y/d = 0) which results in a small slope (note that the HSV extension and the vortex tube on the same side of the cylinder have the same orientation). In the far field of AR = 4, since the vortex tube is located at a higher elevation, the HSV extends downstream with less influence of the vortex tube compared to AR = 1 and 2.

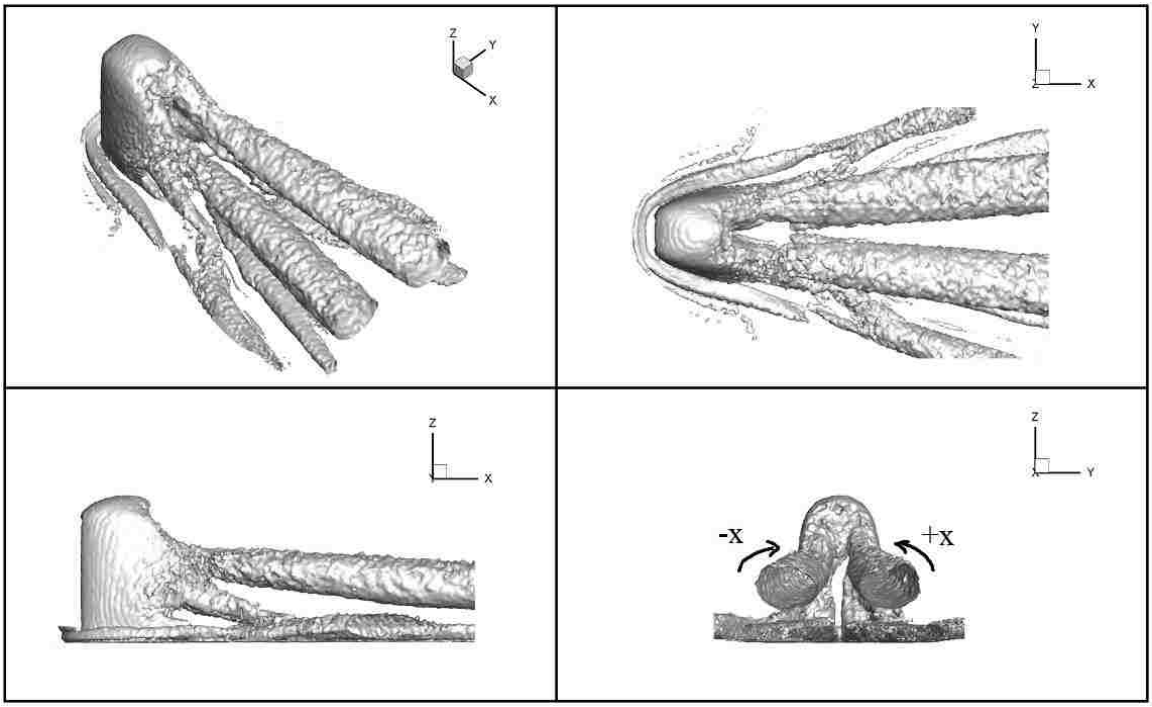

Figure 4.31 Time-averaged λ2 iso-surface of the flow field for AR = 4

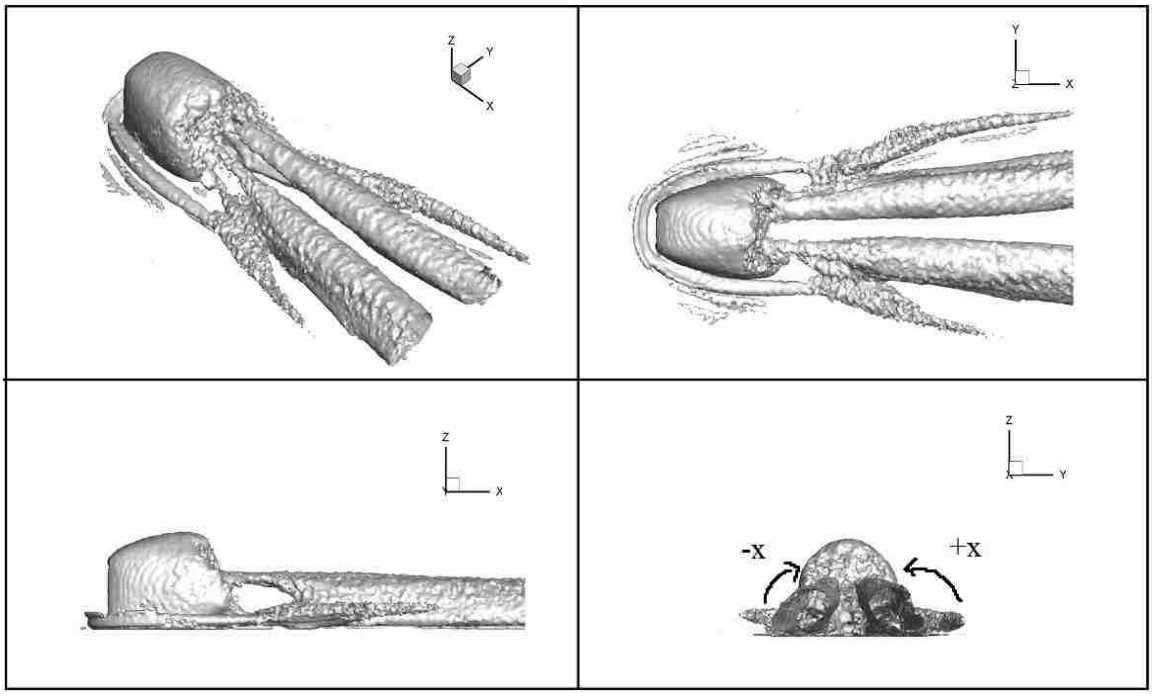

Figure 4.32 Time-averaged λ2 iso-surface of the flow field for AR = 2

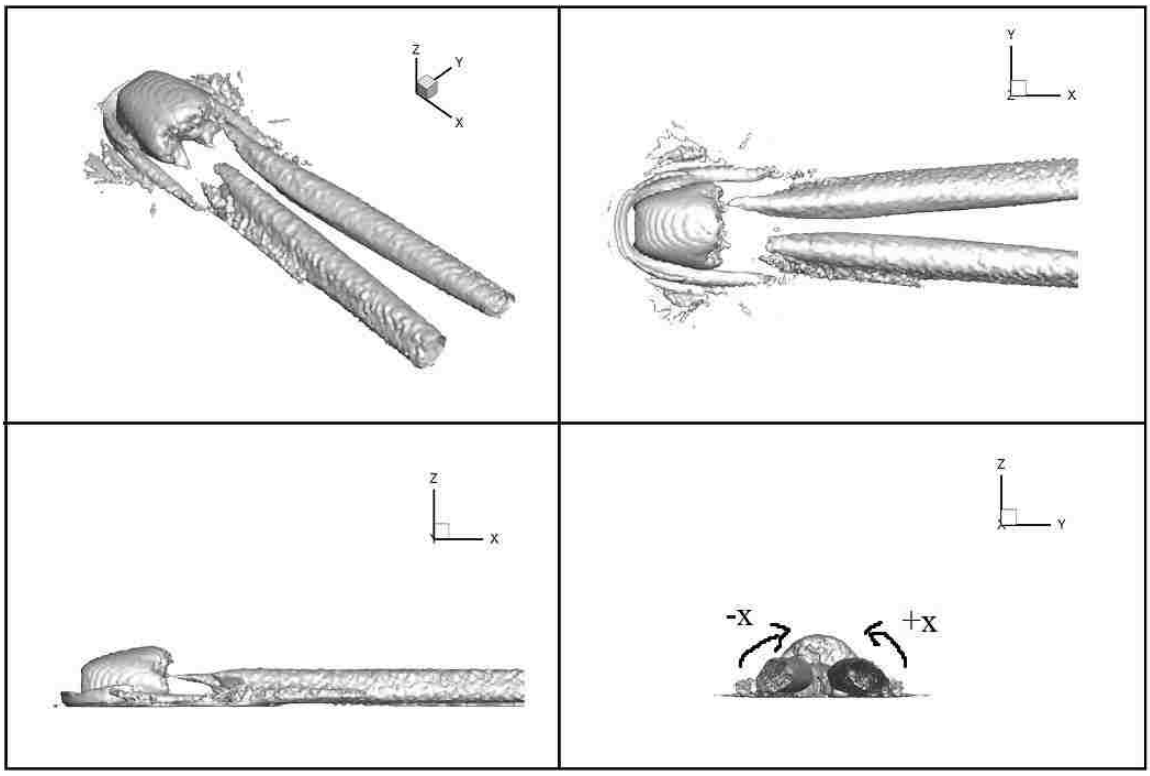

Figure 4.33 Time-averaged λ2 iso-surface of the flow field for AR = 1

Chapter 5 Conclusions and Future Work

5.1 Conclusions

IDDES simulations were conducted in the current study for air flow past a wall-mounted finite-length square cylinder with aspect ratios (AR = h/d) varying from 1 to 4. For the approach flow, a low Reynolds number correction was utilized in the k-ω SST model to better capture the turbulence intensity within the boundary layer. The streamwise velocity, turbulence intensity, and turbulence dissipation rate profiles were mapped onto the inlet boundary of the computational domain for the IDDES simulation of the flow past the bluff body. Grid independence was achieved by testing exponentially decaying values of grid spacing. With the appropriate grid system selection, the simulation results of the flow field for AR = 4 was then validated with experimental results [2], [9] at multiple locations in the wake region.

Vertical planes through y/d = 0 (central plane) and y/d = 0.5 (side-face plane) were used to analyse the flow field in the wake. The time-averaged streamwise velocity contours and the streamtraces showed a recirculation behind the cylinder in each flow field. As the cylinder AR was increased from 1 to 2, the size of the recirculation increased in both the horizontal and vertical directions. As the cylinder AR was further increased to 4, the recirculation maintained its size and an upwash flow was developed under the recirculation. A saddle point was found to occur in the wake of each flow field. The saddle point is located in the near-bed region for AR = 1 and 2, and at z/d = 1 for AR = 4 due to the development of the upwash structure. The orientation of the recirculation was observed to be outward-spiraling (an unsteady focus) in the central plane for AR = 1 and 2, and inward-spiraling vortex (a steady focus) in the central plane of AR = 4.

A new method of horizontal plane selection has been proposed for making comparisons between flow past cylinders with various aspect ratios. Instead of using a geometric parameter such as cylinder height or boundary layer thickness to justify the plane selection, the proposed method selects the horizontal planes based on pressure distribution on the windward face of the body. Two critical points on the pressure distribution plots were introduced: a local minimum close to the bed induced by the horseshoe vortex (Point A) and the maximum pressure at the stagnation point (Point B). By taking the horizontal planes at these two critical points, multiple features in the flow field were discussed, such as the changes in separating shear layer characteristics, horseshoe vortex and wake development. Two other critical points (C and D) were also introduced to better describe the flow field where a constant pressure region exists on the windward face of the bluff body. Point C and Point D are defined as the beginning and the end of the constant pressure region, respectively. Using the proposed method, the differences in the flow fields for AR = 1, 2 and 4 were evaluated and include:

1. Changes in the separating shear layer on the sides of the body due to changes in AR are revealed at the level of both Point A and Point B. As the cylinder AR was increased from 1 to 2, the shear layers on each side were enhanced. However, further increase of the cylinder AR does not affect the separating shear layer.
2. By taking the horizontal plane through Point A in the flow fields, the horseshoe vortices (HSV) and their extensions in the downstream can be compared. As the cylinder AR is increased from 1 to 4, although the HSV was roughly observed to be similar in front of the body, the extension of the HSV was observed to have an increased span and slope.

3. At the level of Point B, the development of the wake in each flow field can be elucidated. The quick transition of the velocity profile from top-hat to Gaussian across the wake for AR = 1 and 4 indicates that the development of the wakes for AR = 1 and 4 were significantly shorter than that for AR = 2, due primarily to the influence of the downwash flow.
4. The horizontal planes at the level of Point C and D may be crucial in flow fields where a constant pressure zone appears on the windward face of the cylinder. It was shown that the incoming flow was strongly influenced by the HSV at the level of Point C and by the separating shear layer at the level of Point D.

In this thesis, flow fields of AR = 1, 2 and 4 were visualized by creating 3-D iso-surfaces of the λ_2. Although the near-wake for each AR was significantly different, the λ_2 criterion indicated that the far-wake of each flow field was similar. Two vortex tubes with streamwise vorticity formed by the separating shear layers from the free-end and sides of the cylinder were observed. The flow fields in the current study were all dipole type, which is different from the quadrupole type observed for cylinders with greater value of AR [3].

5.2 Recommended Future Work

The current study mainly focused on time-averaged quantities to examine the flow fields of each cylinder AR. Bourgeois et al. [25] conducted proper orthogonal deposition (POD) to analyze the flow field of AR = 4 and successfully filtered out the incoherent structures. In the future, POD analysis can be conducted to gain a better knowledge of the flow field for different aspect ratios. Also, as stated in Chapter 4, the flow fields around the cylinder with AR = 1 and 2 were distinctively different from the

flow field for AR = 4. The flow field around the cylinder with higher values of AR can be studied and compared to AR = 4 at Points C and D to further confirm the importance of these two points. Researchers may also take smaller increments in AR to refine the study the effect of aspect ratio on flow past a square cylinder with AR between 2 and 4.

References

[1] C. Lin, T. C. Ho, and S. Dey, "Characteristics of steady horseshoe vortex system near junction of square cylinder and base plate," *Journal of Engineering Mechanics*, vol. 134(2), pp. 184–197, 2008.

[2] M. El Hassan, J. Bourgeois, and R. Martinuzzi, "Boundary layer effect on the vortex shedding of wall-mounted rectangular cylinder," *Experiments in Fluids*, vol. 56(33), 2015.

[3] H. F. Wang and Y. Zhou, "The finite-length square cylinder near wake," *Journal of Fluid Mechanics*, vol. 638, pp. 453-499, 2009.

[4] D. Sumner, "Flow above the free end of a surface-mounted finite-height circular cylinder: A review," *Journal of Fluids and Structures*, vol. 43, pp. 41–63, 2013.

[5] "STAR-CCM V11.04, User Guide." Siemens PLM Software, 2016.

[6] I. P. Castro and A. G. Robins, "The flow around a surface-mounted cube in uniform and turbulent streams," *Journal of Fluid Mechanics*, vol. 79(2), pp. 307-335, 1977.

[7] J. C. R. Hunt, C. J. Abell, J. A. Peterka, and H. Woo, "Kinematical studies of the flows around free or surface-mounted obstacles; applying topology to flow visualization," *Journal of Fluid Mechanics*, vol. 86 pp. 179-200, 1978.

[8] H. F. Wang, Y. Zhou, C. K. Chan, and K. S. Lam, "Effect of initial conditions on interaction between a boundary layer and a wall-mounted finite-length-cylinder wake," *Physics of Fluids*, vol. 18(6), 065106, 2006.

[9] J. A. Bourgeois, P. Sattari, and R. J. Martinuzzi, "Alternating half-loop shedding in the turbulent wake of a finite surface-mounted square cylinder with a thin boundary layer," *Physics of Fluids*, vol. 23(9), 095101, 2011.

[10] K. B. Shah and J. H. Ferziger, “A fluid mechanicians view of wind engineering: Large eddy simulation of flow past a cubic obstacle,” *Journal of Wind Engineering and Industrial Aerodynamics*, vol. 67, pp. 211–224, 1997.

[11] W. Rodi, “Comparison of LES and RANS calculations of the flow around bluff bodies,” *Journal of Wind Engineering and Industrial Aerodynamics*, vol. 69–71, pp. 55–75, 1997.

[12] T. Nishino, G. T. Roberts, and X. Zhang, “Unsteady RANS and detached-eddy simulations of flow around a circular cylinder in ground effect,” *Journal of Fluids and Structures*, vol. 24(1), pp. 18–33, 2008.

[13] G. Nasif, R. Balachandar, and R. M. Barron, “Characteristics of flow structures in the wake of a bed-mounted bluff body in shallow open channels,” *Journal of Fluids Engineering*, vol. 137(10), 101207, 2015.

[14] J. Fröhlich and W. Rodi, “LES of the flow around a cylinder of finite height,” *International Journal of Heat and Fluid Flow*, vol. 25(3), pp. 537–548, 2004.

[15] F. White, *Viscous Fluid Flow*, 3rd ed. Tata Mcgraw Hill, New York City, 2011.

[16] P. R. Spalart, “Detached-eddy simulation,” *Annual Review of Fluid Mechanics*, vol. 41, pp. 181–202, 2009.

[17] D.C. Wilcox, *Turbulence Modelling for CFD*, 2nd ed. DCW Industries, La Cañada, 1994.

[18] F. R. Mentor, “Two-equation eddy-viscosity turbulence modeling for engineering applications,” *AIAA Journal*, vol. 32(8), pp. 1598–1605, 1994.

[19] A. Travin, M. Shur, P. Spalart, and M. Strelets, “On URANS solutions with LES-like behaviour,” *Proceedings of ECCOMAS congress on Computational Methods in Applied Science and Engineering*, Jyväskylä, Finland, July 2004.

[20] P. R. Spalart, S. Deck, M. L. Shur, K. D. Squires, M. K. Strelets, and A. Travin, “A new version of detached-eddy simulation, resistant to ambiguous grid densities,” *Theoretical and Computational Fluid Dynamics*, vol. 20(3), pp. 181–195, 2006.

[21] M. Saeedi and B.-C. Wang, “Large-eddy simulation of turbulent flow around a finite-height wall-mounted square cylinder within a thin boundary layer,” *Flow, Turbulence and Combustion*, vol. 97(2), pp. 513–538, 2016.

[22] J. Franke, A. Hellsten, H. Schlünzen, and B. Carissimo, *Best Practice Guideline For The CFD Simulation of Flows In The Urban Environment*, COST Office, Brussels, 2007.

[23] P. Spalart, “Direct simulation of a turbulent boundary layer up to $R_\theta = 1410$,” *Journal of Fluid Mechanics*, vol. 187, pp. 61–98, 1988.

[24] J. A. Bourgeois, B. R. Noack, and R. J. Martinuzzi, “Generalized phase average with applications to sensor-based flow estimation of the wall-mounted square cylinder wake,” *Journal of Fluid Mechanics*, vol. 736, pp. 316–350, 2013.

[25] A. Okajima, “Strouhal numbers of rectangular cylinders,” *Journal of Fluid Mechanics*, vol. 123(1), pp. 379- 398, 1982.

[26] M. M. Zdravkovich, *Flow Around Circular Cylinders, vol 2: Applications*. Oxford University Press, Oxford, 2003.

[27] M. Heidari, “Wake characteristics of single and tandem emergent cylinders in shallow open channel flow,” PhD dissertation, University of Windsor, 2016.

[28] A. E. Perry and B. D. Fairlie, “Critical points in flow patterns,” *Advances in Geophysics*, vol. 18, pp. 299–315, 1975.

[29] R. Vinuesa, P. Schlatter, J. Malm, C. Mavriplis, and D. S. Henningson, “Direct numerical simulation of the flow around a wall-mounted square cylinder under various inflow conditions,” *Journal of Turbulence*, vol. 16(6), pp. 555–587, 2015.

[30] H. Akilli and D. Rockwell, “Vortex formation from a cylinder in shallow water,” *Physics of Fluids*, vol. 14(9), pp. 2957–2967, 2002.

[31] J. Jeong and F. Hussain, “On the identification of a vortex,” *Journal of Fluid Mechanics*, vol. 285(1), pp. 69-94, 1995.

Vita Auctoris

Name: Junting Chen

Place of Birth: Tianjin, China

Year of Birth: 1990

Education: University of Windsor, Windsor

2010 – 2015 B.A.Sc